Computers and Structures 218 (2019) 60–81

Contents lists available at ScienceDirect

Computers and Structures

journal homepage: www.elsevier.com/locate/compstruc

On the material and material-adapted approaches to curve framing with applications in path estimation, shape reconstruction, and computer graphics

Mayank Chadha, Michael D. Todd *

Department of Structural Engineering, University of California, San Diego, 9500 Gilman Drive 0085, La Jolla, CA 92093-0085, United States

ARTICLE INFO

Article history:
Received 26 November 2018
Accepted 27 March 2019
Available online 8 April 2019

Keywords:
Curve framing
Material-adapted frame
Material frame
Computer graphics
Path estimation
Shape reconstruction

ABSTRACT

In this paper, we investigate an approach towards curve framing using material frames (MF). Motivated from the successful application of MF in shape sensing of rods in our previous work, we now present these frames as an alternative curve framing method. There are numerous instances of practical importance, where the dynamic system in consideration can be geometrically modeled by means of framed space curve. Unlike the Frenet-Serret and relatively parallel adapted frames (RPAF), the MF is conveniently defined in terms of the parameters associated with the system configuration.

We detail the construction of the various material frames. We develop the relationships among the MF, Frenet frame, and the RPAF. We discuss the estimation of state space of the system from a limited set of material curvature and velocity data. In one of the approaches discussed, we obtain curvature-dependent shape functions to estimate the framed curve globally and discuss the errors associated with such estimations.

We also describe the potential strengths of framed space curves in the reconstruction of slender structures, trajectory estimation of moving objects (like drone swarms), and in computer graphics. We do this by creating an analogy between the non-linear geometry of Cosserat beams and these applications.

1. Introduction

The space curves are the simplest structures in the theory of differential geometry because they are manifolds of dimension one. The interest in space curves dates back to 17th century. The idea of tangent to the curve is attributed to Pierre De Fermat that was first mentioned in 1629 in a letter to M. Despagnet. It seemingly was invented as a side product of Fermat's investigation on maxima and minima (refer to [1]). In 1637, Descartes was the first to define the algebraic curve in his famous work [2]. In 1748, Euler used the parametric representation of curves in his renowned work [3]. The idea of curve framing by means of tangent, normal, and binormal vectors are attributed to Frenet [4] and Serret [5]. Darboux [6] exploited the moving frame technique to study surfaces, which was further generalized by Cartan (refer to: for example, [7,8]) and it was used to develop tetrad theory of general relativity [9]. Under the Frenet-Serret curve framing technique, the curve is geometrically characterized by means of coordinate system invariant quantities: *curvature* $\overline{\kappa}$ and *torsion* $\overline{\tau}$. A unique Frenet frame exists for a regular, at least C^3 continuous and non-degenerate curve.

Despite the fact that a Frenet–Serret formulation is at the heart of curve framing, it has limitations for certain practical problems and applications such as (but not limited to) graphics generation, shape reconstruction from finite strain measurements, modeling the trajectory and motion of certain classes of moving objects, defining the configuration of object swarms, modeling the continuum mechanics of Cosserat beams, and so forth. These applications demand the existence of a continuously varying frame along the curve, even if the curvature vanishes at certain point on the curve. The principal normal of the curve is discontinuous at the point where the curvature is 0 (point of inflection or when the curve straightens momentarily), rendering a limitation to use of the Frenet frame for these applications.

Bishop [10] proposed an alternative framing methodology called *relatively parallel adapted frame* (RPAF). RPAF can be used to frame a regular, minimally C^2 continuous curve using two invariants say $(\overline{\kappa}_1, \overline{\kappa}_2)$ that can be uniquely defined if we specify the orthogonal vectors spanning the normal plane of such a curve at a particular point on it. Bishop called the invariants $(\overline{\kappa}_1, \overline{\kappa}_2)$ as

* Corresponding author.
E-mail addresses: machadha@eng.ucsd.edu (M. Chadha), mdtodd@ucsd.edu (M.D. Todd).

https://doi.org/10.1016/j.compstruc.2019.03.011
0045-7949/

the *normal development* of the curve. Like the Frenet frame, we only have two invariants in RPAFs that define the curve. The curve still needs to be regular, but the requirements of continuity and the non-degeneracy condition of the curve are relaxed.

The benefit of RPAF has been proven since its proposal in 1975. The application of RPAF in computer graphics to create ribbons, tubes from 3D space curves, and the generation of forward-facing camera orientation was investigated by Hanson and Ma [11]. The RPAF has successfully been used to develop trajectory tracking and auto-pilot control system for UAVs (refer Fig. 1 in Xargay et al. [12] and references therein). The work by Zahradová [13] used RPAF to construct waveguides for curves that did not possess unique Frenet frames.

The Frenet frames and RPAF are intrinsic to the curve itself. Therefore, the curvature terms $(\overline{\kappa}, \overline{\tau})$ in case of Frenet frame and the terms $(\overline{\kappa}_1, \overline{\kappa}_2)$ in case of a unique RPAF are frame invariants and depend solely on the properties of the curve. However, in multiple practical applications where a physical system can be modeled by means of framed curve, it is convenient to frame the curve by means of the *material frame* (MF). The evolution of the MF along the curve depends on the configuration-dependent parameters. When MF includes the tangent vector of the curve, it is called as *material-adapted frame* (MAF). The curvatures related to such frames usually have a physical meaning associated with the change of state of the system. One of the best example to justify the importance of the MF is the kinematics of rods and beams (slender structures).

The inception of the idea to use framed curves in studying the mechanics of rods is likely attributed to Duhem [14] and was used by Cosserat and Cosserat [15] to develop the finite strain theory of rods and shells. In this framework, a configuration of the beam is defined by the midcurve (locus of centroid of the cross-section) and the family of cross-sections given by the director frame field (also known as the *Cosserat triad*). The director triad is an example of MF used to frame Cosserat beams, for example. Interested readers are recommended to refer to Chadha and Todd [16], Ericksen and Truesdell [17] and the references therein for further details. The contribution of Simo (refer to: for example, [18]) and Eric Reissner (refer to [19]) on the development of geometrically-exact non-linear beam theory is noteworthy. The idea to capture the three-dimensional shape of slender rod-like structure subjected to bending and elongation using a finite number of surface strain gauges was proposed by Todd et al. [20] using MAF. Chadha and Todd [21] extended the work in [20] by developing a general shape reconstruction theory that captures shear deformations and torsion by using a director triad. The geometric relationship between MAF and director triad was used to uniquely define orientation of cross-section and the shear angles (refer to Section 3.2 of Chadha and Todd [16]). It was also proved that the director triad reduces to MAF when shear deformation and torsion is ignored. The fact that the Frenet-Serret frame and the RPAF do not materially change orientation with the cross-section during the deformation of the beam, motivated Todd et al. [20] to propose a problem-specific MAF (we will later call this as special material adapted frame or SMAF as it ignores torsion and this adds some interesting properties to this frame). This also makes it favorable to define geometry of single-manifold characterizable structures like DNA, tubes with continuously varying cross-section, architectural design of spiral stair case and their handrails where the central column is not necessarily a vertical element, and body-centered frame for fixed wings airplanes to name a few.

Motivated from the success of a MAF in the theory of shape reconstruction, we attempt to further investigate the properties of MAF and explore its potential applications in the field of computer graphics and path estimation (for drones and swarms of drones, for example). In this exposition, we systematically elucidate the construction of the MAF and establish the relationship between MAF, Frenet frame, and RPAF. We finally detail the general material frame. We illustrate the application of these frames towards generation of certain structures: double helix intertwining a space curve (like DNA), a leaf and a plant.

We derive the evolution equations of the material frames and illustrate an algorithm to estimate a smooth framed curve using limited set of curvature data. This estimation technique is very useful for structural monitoring of slender structures like pipelines or for path estimation of underwater drones, where the data is scarce due to challenges associated with underwater communication. We illustrate various interpolation approaches. One of the approaches that has a closed form solution is *smooth patch estimation and gluing technique* (SPEG) that involves C^{-1} estimation of the material linear and angular velocity data (or equivalently cross-sectional strain and curvature in case of beam). We develop curvature-dependent local shape functions (for a given segment or patch of the curve) and "glue" these patches together such that the global solution obtained is smooth. Other higher order interpolation of the input curvature data to numerically obtain the configuration space is also discussed. The accuracy of the estimated curve depends on the quality of curvatures data set and the interpolation method that was used to estimate the path. We illustrate application of this algorithm to estimate the path of a moving object or swarm of drones using limited set of data obtained from the sensors (like Inertial Measurement Units (IMU), strain gauges, etc.).

In Section 2, we briefly describe the Frenet frame and RPAF. We delineate the construction of the MF and discuss the concept of finite rotations in Section 3. In Section 4, we derive the curvature vector for various frames and obtain the required constraints for Frenet frame and RPAF to be a special case of GMAF. In Section 5, we delineate the estimation of the state space of a single-manifold characterized system from limited material tangent data. We also perform error analysis for different interpolation approaches. In Section 6, we illustrates various applications of theory discussed so far in the field of computer graphics, and we finally draw some conclusions and primary observations in Section 7.

2. Curve framing by Frenet-Serret frame and RPAF

In this section, we briefly review the concepts of Frenet frame and RPAF and discuss the relevant concepts for completion. Unless otherwise stated, the curves are parametrized using arc-length ξ_1 throughout the paper. The dot product between two vectors $\boldsymbol{v}_1$ and $\boldsymbol{v}_2$ is defined as $\langle \boldsymbol{v}_1, \boldsymbol{v}_2 \rangle$.

2.1. Frenet-Serret frame

Consider a fixed orthonormal Cartesian frame $\{\mathbf{E}_i\}$ in Euclidean space $\mathbb{R}^3$. Consider a *non-degenerate* and at least C^3 continuous space curve $\boldsymbol{\varphi} : [0, l_0] \to \mathbb{R}^3$, such that, $\boldsymbol{\varphi}(\xi_1) = \varphi_i(\xi_1)\mathbf{E}_i$, with the arclength $\xi_1 \in [0, l_0]$. Uniquely framing a curve using Frenet frame requires a continuously varying Frenet triad consisting of tangent $\boldsymbol{T}(\xi_1)$, principal normal $\boldsymbol{N}(\xi_1)$, and binormal vectors $\boldsymbol{B}(\xi_1)$ defined as

$$\begin{aligned} \boldsymbol{T}(\xi_1) &= \boldsymbol{\varphi}_{,\xi_1}; \\ \boldsymbol{N}(\xi_1) &= \frac{\boldsymbol{\varphi}_{,\xi_1\xi_1}}{\|\boldsymbol{\varphi}_{,\xi_1\xi_1}\|}; \\ \boldsymbol{B}(\xi_1) &= \boldsymbol{T}(\xi_1) \times \boldsymbol{N}(\xi_1). \end{aligned} \tag{1}$$

The vector triad $\{\boldsymbol{T}(\xi_1), \boldsymbol{N}(\xi_1), \boldsymbol{B}(\xi_1)\}$ as given in Eq. (1) defines the Frenet frame. Before we mention the Frenet formula that governs the evolution of the Frenet triad, we make the following remarks

that are required to understand the unique existence and continuity requirement of the frame.

Remarks:

Remark 2.1.1. A parametrized C^1 continuous curve $\boldsymbol{\varphi}(\xi_1)$ is called a *regular curve* if it has a non-vanishing derivative. This guarantees the existence of non-zero and continuous tangent vector field $\boldsymbol{T}(\xi_1)$. A regular curve parametrized by the arc-length ξ_1 gives a unit tangent vector, i.e. $\|\boldsymbol{\varphi}_{,\xi_1}\| = 1$.

Remark 2.1.2. For a parametrized C^2 continuous curve $\boldsymbol{\varphi}(\xi_1)$, we define the scalar curvature $\overline{\kappa}(\xi_1) = \|\boldsymbol{\varphi}_{,\xi_1\xi_1}\|$. The point on the curve at which the curvature vanishes $\overline{\kappa} = 0$, is called as the *inflection point*. The point with $\overline{\kappa} \neq 0$ on a regular curve is called as a *strongly regular* point. At the point of inflection, the curve is momentarily straight and the normal vector is not uniquely defined. Thus, the Frenet frame consisting of unique principal normal does not exist at the *point of inflection*.

Remark 2.1.3. At a *strongly regular* point of C^2 continuous curve with $\overline{\kappa}(\xi_1) \neq 0$, the tangent $\boldsymbol{T}$ and the principal normal vector $\boldsymbol{N}$ are linearly independent (orthonormal) and spans the *osculating plane*. This condition is called as *non-degeneracy*. The normal vector points towards the *center of curvature*. The circle on the osculating plane centered at the *center of curvature* with the radius $\frac{1}{\overline{\kappa}}$ is called as the *osculating circle*. A regular C^2 curve with $\overline{\kappa}(\xi_1) \neq 0$ (implying linear independence of $\boldsymbol{T}$ and $\boldsymbol{N}$) is called as *non-degenerate* curve. The curvature $\overline{\kappa}(\xi_1)$ measures the rate of change of the tangent when moving along the curve. It represents the deviation of the curve at a point from a straight line (along the tangent at a point) in the neighborhood of the point in consideration.

Remark 2.1.4. The binormal vector $\boldsymbol{B}$ as defined in Eq. (1) is perpendicular to the *osculating plane*. The plane spanned by the vectors $\boldsymbol{T}$ and $\boldsymbol{B}$ is called as the *rectifying plane*. For the Frenet frame to be continuous along the curve, the osculating plane must change continuously along the curve. This brings us to the definition of *torsion* $\overline{\tau}(\xi_1)$. The deviation of the osculating plane is obtained from the derivative of the binormal vector, which can be obtained as $\boldsymbol{B}_{,\xi_1} = -\overline{\tau}\boldsymbol{N}$ (refer Chapter II of Kreyszig [22]). The continuity of the Frenet frame along the curve requires the vector $\boldsymbol{B}_{,\xi_1}$ to be at least C^0 continuous, implying the curve $\boldsymbol{\varphi}(\xi_1)$ to be at least C^3 continuous. The C^2 continuity of a non-degenerate curve implies the existence of osculating circle (curvature continuity) and the C^3 continuity of such curve implies that osculating circle or osculating plane changes smoothly (torsion continuity).

The Frenet-Serret formulas represent the first derivatives of vectors $\boldsymbol{T}_{,\xi_1}, \boldsymbol{N}_{,\xi_1}$ and $\boldsymbol{B}_{,\xi_1}$ as a linear combination of the Frenet triad as is shown below

$$\begin{bmatrix} \boldsymbol{T}_{,\xi_1} \\ \boldsymbol{N}_{,\xi_1} \\ \boldsymbol{B}_{,\xi_1} \end{bmatrix} = \begin{bmatrix} 0 & \overline{\kappa} & 0 \\ -\overline{\kappa} & 0 & \overline{\tau} \\ 0 & -\overline{\tau} & 0 \end{bmatrix} \begin{bmatrix} \boldsymbol{T} \\ \boldsymbol{N} \\ \boldsymbol{B} \end{bmatrix}. \tag{2}$$

The Frenet triad continuously moves along the curve. If the Frenet triad is obtained by finite rotation of the fixed triad $\{\boldsymbol{E}_i\}$, we have

$$\boldsymbol{Q}_{\mathrm{f}} = \boldsymbol{T} \otimes \boldsymbol{E}_1 + \boldsymbol{N} \otimes \boldsymbol{E}_2 + \boldsymbol{B} \otimes \boldsymbol{E}_3. \tag{3}$$

The tensor $\boldsymbol{Q}_{\mathrm{f}}(\xi_1)$ represents the family of orthogonal tensors belonging to the $SO(3)$ rotational Lie groups. From Eq. (3), the following holds

$$\begin{aligned} \boldsymbol{T}_{,\xi_1} &= \boldsymbol{Q}_{\mathrm{f},\xi_1}\boldsymbol{Q}_{\mathrm{f}}^T\boldsymbol{T} = \boldsymbol{\kappa}_{\mathrm{f}} \times \boldsymbol{T}; \\ \boldsymbol{N}_{,\xi_1} &= \boldsymbol{Q}_{\mathrm{f},\xi_1}\boldsymbol{Q}_{\mathrm{f}}^T\boldsymbol{N} = \boldsymbol{\kappa}_{\mathrm{f}} \times \boldsymbol{N}; \\ \boldsymbol{B}_{,\xi_1} &= \boldsymbol{Q}_{\mathrm{f},\xi_1}\boldsymbol{Q}_{\mathrm{f}}^T\boldsymbol{B} = \boldsymbol{\kappa}_{\mathrm{f}} \times \boldsymbol{B}. \end{aligned} \tag{4}$$

For an orthogonal matrix $\boldsymbol{Q}_{\mathrm{f}}$, it can be proven that $\boldsymbol{Q}_{\mathrm{f},\xi_1}\boldsymbol{Q}_{\mathrm{f}}^T$ is an anti-symmetric matrix. Therefore, there exists a corresponding axial vector $\boldsymbol{\kappa}_{\mathrm{f}}$ such that Eq. (4) holds. The vector $\boldsymbol{\kappa}_{\mathrm{f}} = \overline{\tau}\boldsymbol{T} + \overline{\kappa}\boldsymbol{B}$ is called as the *Darboux vector* (refer Chapter II of Kreyszig [22]). It can also be interpreted as a rotation vector of the Frenet triad for a non-degenerate C^3 continuous curve $\boldsymbol{\varphi}(\xi_1)$ causing infinitesimal rotation of the triad as we move along the curve. Finally we present the formula for the frame invariants $(\overline{\kappa}, \overline{\tau})$,

$$\begin{aligned} \overline{\kappa}(\xi_1) &= \frac{\|\boldsymbol{\varphi}_{,\xi_1} \times \boldsymbol{\varphi}_{,\xi_1\xi_1}\|}{\|\boldsymbol{\varphi}_{,\xi_1}\|^3}; \\ \overline{\tau}(\xi_1) &= \frac{\left\langle \left(\boldsymbol{\varphi}_{,\xi_1} \times \boldsymbol{\varphi}_{,\xi_1\xi_1}\right), \left(\boldsymbol{\varphi}_{,\xi_1\xi_1\xi_1}\right) \right\rangle}{\|\boldsymbol{\varphi}_{,\xi_1} \times \boldsymbol{\varphi}_{,\xi_1\xi_1}\|^2}. \end{aligned} \tag{5}$$

Fig. 1 illustrates the construction discussed above.

2.2. Relatively parallel adapted frame: Bishop's frame

As explained in the last section, a curve may be uniquely framed by Frenet triad if it is non-degenerate and at least C^3 continuous. Bishop [10] proposed an alternative curve framing approach that relaxes the continuity requirement among others. For a curve to be framed by RPAF, it needs to be at least C^2 continuous and regular. We present an argument that justifies the construction of RPAF.

Let us consider a regular and at least C^2 continuous curve. Such a curve guarantees a non-zero tangent vector. The idea is to device a method to span the plane perpendicular to the tangent vector (*normal plane*) such that the two vector fields spanning the normal plane and the tangent vector forms an orthonormal triad that is continuously varying along the curve. Therefore, we first define a *normal vector field* as the vector field that is perpendicular to the tangent vector $\boldsymbol{T}(\xi_1)$ of the curve $\boldsymbol{\varphi}(\xi_1)$. Let χ represent set of all the continuous normal vector field. The aim is to obtain a *unique* pair of *orthonormal vector fields* $\boldsymbol{N}_1(\xi_1), \boldsymbol{N}_2(\xi_1) \in \chi$ spanning the normal plane. For the construction of the triad, we assume that the normal vector fields $\boldsymbol{N}_1(\xi_1)$ and $\boldsymbol{N}_2(\xi_1)$ are perpendicular to each other. Bishop proposed that the normal vector fields $\boldsymbol{N}_1(\xi_1)$ (or $\boldsymbol{N}_2(\xi_1)$) can be obtained if the total derivative $\frac{\mathrm{d}\boldsymbol{N}_i}{\mathrm{d}\xi_1} = \boldsymbol{N}_{i,\xi_1}$ is parallel to the tangent vector field $\boldsymbol{T}(\xi_1)$ for $i = 1, 2$. The uniqueness of this field can be guaranteed by fixing the normal vectors at a fixed arclength ξ_{10} such that $\boldsymbol{N}_i(\xi_{10}) = \boldsymbol{N}_{i0}$ (called as *generators*). Let us call this as the *uniqueness criterion* and the vector $\boldsymbol{N}_{i0}$ as the *generator*.

The vector field $\boldsymbol{N}_i(\xi_1) \in \chi$ is called as *relatively parallel normal field* if $\boldsymbol{N}_{i,\xi_1}$ is parallel to the tangent vector $\boldsymbol{T}(\xi_1)$. Theorem 1 in Bishop [10] gives continuity and uniqueness requirement of relatively parallel normal fields. The frame consisting of the tangent vector $\boldsymbol{T}(\xi_1)$ and two unique relatively parallel orthonormal fields $\boldsymbol{N}_1(\xi_1), \boldsymbol{N}_2(\xi_1) \in \chi$ is called as *relatively parallel adapted frame* (RPAF). Theorem 2 in Bishop [10] defines the family of RPAF (we can obtain a unique frame by invoking the *uniqueness criterion*). If $\{\boldsymbol{T}, \boldsymbol{N}_1, \boldsymbol{N}_2\}$ is a RPAF, we have,

$$\begin{bmatrix} \boldsymbol{T}_{,\xi_1} \\ \boldsymbol{N}_{1,\xi_1} \\ \boldsymbol{N}_{2,\xi_1} \end{bmatrix} = \begin{bmatrix} 0 & \overline{\kappa}_1 & \overline{\kappa}_2 \\ -\overline{\kappa}_1 & 0 & 0 \\ -\overline{\kappa}_2 & 0 & 0 \end{bmatrix} \begin{bmatrix} \boldsymbol{T} \\ \boldsymbol{N}_1 \\ \boldsymbol{N}_2 \end{bmatrix}. \tag{6}$$

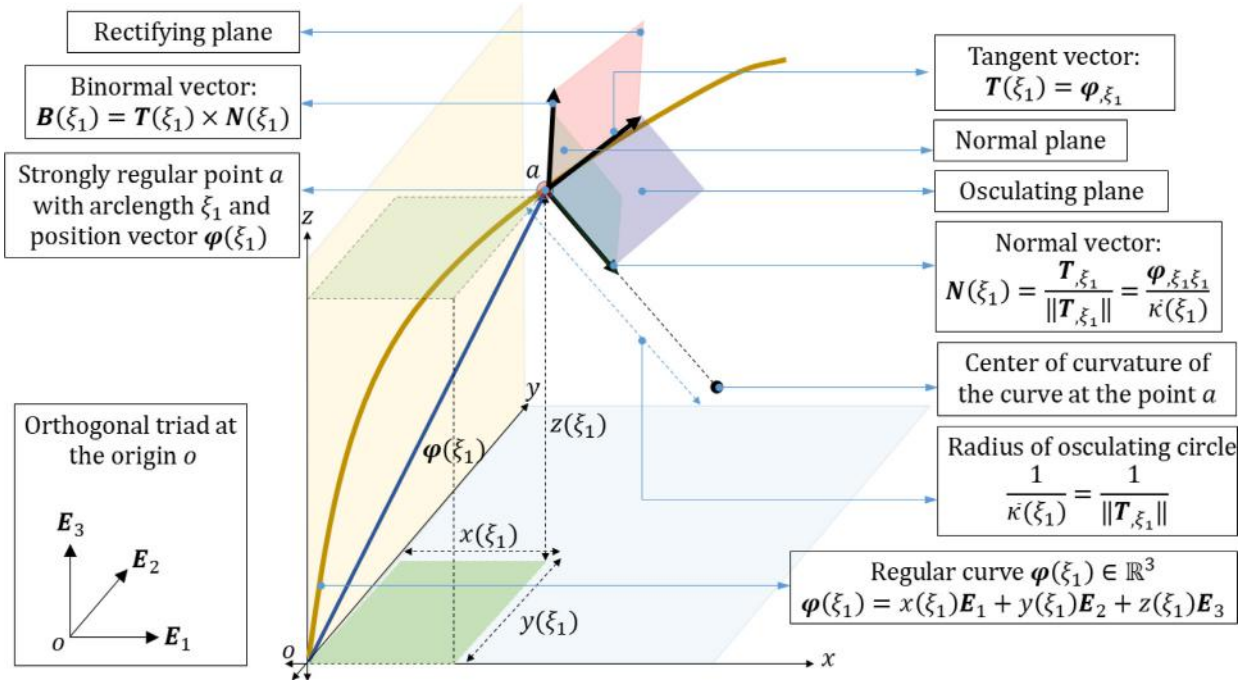

Fig. 1. Frenet-Serret frame.

It is thus clear that if the regular curve $\boldsymbol{\varphi}$ is C^r continuous with $r \geqslant 2$, the tangent vector is C^{r-1} continuous. Using Eq. (6), this fact implies that the normal fields are C^{r-1} continuous (refer Theorem 1 in Bishop [10]). The parameters $(\overline{\kappa}_1, \overline{\kappa}_2)$ governs the evolution of the RPAF and are determined uniquely up to rotation (for *properly oriented* frame). These parameters can be determined uniquely by invoking the *uniqueness criterion* defined above and are called as the *normal development* of the curve $\boldsymbol{\varphi}$. The *Darboux vector* corresponding to RPAF is $\boldsymbol{\kappa}_b = \overline{\kappa}_1 \boldsymbol{N}_2 - \overline{\kappa}_2 \boldsymbol{N}_1$.

For a regular non-degenerate and at least C^3 curve, the relationship between Frenet frame and the RPAF can be summarized as (refer Bishop [10]),

$$\overline{\kappa}^2 = \overline{\kappa}_1^2 + \overline{\kappa}_2^2; \tag{7a}$$

$$\overline{\tau} = \eta_{,\xi_1}; \tag{7b}$$

$$\eta = \arctan\frac{\overline{\kappa}_2}{\overline{\kappa}_1}. \tag{7c}$$

Here, η represents the angular deviation of the vectors $\boldsymbol{N}$ and $\boldsymbol{B}$ from the vectors $\boldsymbol{N}_1$ and $\boldsymbol{N}_2$ respectively measured in clockwise direction (refer Fig. 2).

Remarks:

Remark 2.2.1. An arbitrary vector field is relatively parallel if its tangential component is a constant multiple of the unit tangent field $\boldsymbol{T}(\xi_1)$ and its normal component is relatively parallel in the sense discussed above.

Remark 2.2.2. In differential geometry, there is a notion of *parallel-transport*, in which, a geometric object (say a vector) is said to be parallel transported along a curve in a manifold if its covariant derivative vanishes (refer chapter 2 of Do Carmo [23]). Two parallel-transported vector fields do preserve length and relative orientation in Riemannian manifold. However, it must be noted that the relatively parallel vector field, say $\boldsymbol{M}(\xi_1)$, is not obtained by *parallel-transport* of the normal vector $\boldsymbol{M}(\xi_{10}) = \boldsymbol{M}_{10}$ along the curve. Therefore, in our opinion, it is inappropriate and misleading to call RPAF as *parallel-transport frame*.

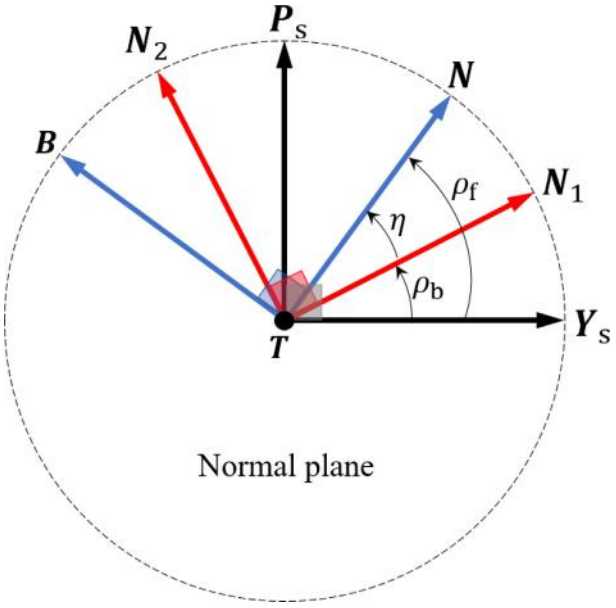

Fig. 2. Orientation of various adapted frames in the normal plane.

3. Material frames and finite rotations

3.1. Motivation

In numerous practical applications the idea of curve framing is very useful to model the geometry of the system. Many a times, the frame is required to be attached to the system, thus justifying the word "material" in *Material frames* (MF). The configuration of such system is defined by a curve and the frame attached to the curve. If the frame consist of the tangent vector of the curve as one of three orthogonal vectors, it is called as "adapted" frame. We shall see in a while that there are systems that requires a more general frame that are attached to the curve but does not contain tangent vector

as a part of the triad (for example, a general director triad). Those are still "material" frames, but not "material-adapted" frames. Unlike Frenet frame or the RPAF, the orientation of these frames depends on the parameters defining the configuration of the system under consideration. Let us explain the idea of "material adapted" frame with some examples.

Consider the non-linear large deformation of a cantilever beam subjected to pure bending (no shear deformation) and elongation. Such a structure may be modeled by a curve (called the midcurve, obtained by joining the cross-sectional centroidal loci along the rod) and the family of rigid cross-sections. Euler-Bernoulli beam theory assumes bending as the predominant cause of deformation and ignores shear and other inplane and out of plane deformations. For such a case, bending guarantees that the cross-sections of the rod is perpendicular to the tangent vector of the midcurve, or in other words, the cross-sections lie on the normal plane of the curve at any deformed configuration. This is also valid for non-linear Kirchhoff-Love beams that constraints the cross-section to be perpendicular to the midcurve. Thus, we need a material-adapted frame to model such a rod (as we shall see later, this frame will be called as *special material adapted frame* SMAF). Todd et al. [20] in their first work on shape reconstruction used SMAF because bending curvatures and elongation dominate the overall contributions to deformation in case of slender rods.

Consider a similar rod subjected to torsion along with the bending and elongation. The cross-sections still lie on the normal plane but they are subjected to rotation about the tangent vector. Consider another example of a fixed wing airplane that has three degrees of freedom in rotation. The configuration of an airplane can be modeled by a curve parametrized with time. The normalized tangent vector of such curve is along the *roll axis*, whereas the *pitch axis* and *yaw axis* span the normal plane. We call these kind of frames as *general material adapted frame* (GMAF). If the roll angle in case of airplane and the torsion deformation in case of rods vanish, the GMAF reduces to SMAF. In other words, GMAF can be obtained from SMAF by orthogonal rotation about the tangent vector.

Finally, consider a general example of rod deformation. Let us subject the rod to shear deformation along with all the other effects discussed before. Inclusion of shear deformation relaxes the constraint of the cross-section to lie on the normal plane. Therefore, to model such a structure, we need a frame that contains a vector perpendicular to the cross-section (need not be along the tangent vector of the curve) and a pair of orthogonal vectors to span the cross-section (that need not lie on the normal plane but still is subjected to rigid cross-section assumption). Chadha and Todd [21,24] used this framing technique (in this case we used *Cosserat frame*) to generalize the theory of shape sensing to include shear deformations and Poisson's inplane cross-sectional deformation among other effects. In general, we call this frame as *material frame* (MF) and not MAF because the tangent vector is not a part of triad anymore.

Another interesting application of MF can be realized in the design of a spiral staircase. If the central column is straight (which is usually the case in practical designs), the tread falls on the normal plane of the column and the hand rail is perfectly spiral, thus MAF is apt to describe such a geometry. However, if the central column is slightly deviated or inclined due to construction requirement, the tread may no longer be on the normal plane and secondly, the handrail will not be a perfect spiral anymore. We would need MF to address such geometries.

3.2. Finite rotations: rotation matrix and rotation tensor

In practical applications, the material frames are obtained by finite rotation of the triad $\{\boldsymbol{E}_i\}$. For instance, the Inertial Measurement Unit (IMU) of a dynamic system are always initially calibrated with respect to some fixed triad, say $\{\boldsymbol{E}_i\}$. Before we construct various material frames, we briefly describe finite rotation of a vector and an orthonormal triad.

3.2.1. Rotation of a vector: rotation tensor

The rotation tensor belong to a *proper orthogonal rotation group* $SO(3)$. The $SO(3)$ manifold is a compact Lie group having skew-symmetric matrix as its Lie algebra, $so(3)$. The Lie algebra to $SO(3)$ represents its tangent plane at the identity element of $SO(3)$.

Consider a vector $\boldsymbol{V}_\mathrm{i}$ that is to be rotated to $\boldsymbol{V}_\mathrm{f}$ by a proper orthogonal tensor $\boldsymbol{Q} \in SO(3)$ such that, $\boldsymbol{V}_\mathrm{f} = \boldsymbol{Q}\boldsymbol{V}_\mathrm{i}$. The component of the tensor $\boldsymbol{Q}$ represented by the matrix $[\boldsymbol{Q}]_{\boldsymbol{E}_i \otimes \boldsymbol{E}_j} = Q_{ij}(\boldsymbol{E}_i \otimes \boldsymbol{E}_j)$ has three independent entries because of the orthogonality constraint: $\boldsymbol{Q}^T\boldsymbol{Q} = \boldsymbol{I}_3$. Therefore, $\boldsymbol{Q}$ can be parametrized by three parameters or a vector in $\mathbb{R}^3$. There are multiple ways for the parametrization of the rotation tensor. We focus on three of them: the Euler Angles, the quaternions and the Rodrigues rotation formula. We omit the description of Euler angles (that deals with sequential rotations) for they are straight forward and common. However, we briefly describe the quaternion approach and Rodrigues rotation formula.

3.2.1.1. Rodrigues rotation formula. We first describe Rodrigues rotation approach for finite rotations. The vector $\boldsymbol{V}_\mathrm{f}$ can be obtained by rotation of the vector $\boldsymbol{V}_\mathrm{i}$ about the unit vector $\boldsymbol{n}_\theta = n_{\theta i}\boldsymbol{E}_i$ by an angle θ. This enables us to parametrize the rotation tensor $\boldsymbol{Q}$ by means of a vector $\boldsymbol{\theta} = \theta\boldsymbol{n}_\theta$, such that $\boldsymbol{V}_\mathrm{f} = \boldsymbol{Q}(\boldsymbol{\theta})\boldsymbol{V}_\mathrm{i}$. By Rodrigues formula,

$$\boldsymbol{V}_\mathrm{f} = [\boldsymbol{V}_\mathrm{i} + \boldsymbol{n}_\theta \times \boldsymbol{n}_\theta \times \boldsymbol{V}_\mathrm{i}] + [\boldsymbol{n}_\theta \times \boldsymbol{V}_\mathrm{i}]\ \sin\theta - [\boldsymbol{n}_\theta \times \boldsymbol{n}_\theta \times \boldsymbol{V}_\mathrm{i}]\ \cos\theta. \tag{8}$$

If $\boldsymbol{\Theta} \in so(3)$ represents the spin matrix with the corresponding axial vector $\boldsymbol{\theta} = \theta(n_{\theta i}\boldsymbol{E}_i) = \theta_i\boldsymbol{E}_i$, we have,

$$\boldsymbol{\Theta}(\boldsymbol{\theta}) = \theta\begin{bmatrix} 0 & -n_{\theta 3} & n_{\theta 2} \\ n_{\theta 3} & 0 & -n_{\theta 1} \\ -n_{\theta 2} & n_{\theta 1} & 0 \end{bmatrix}. \tag{9}$$

We state a useful property associated with Eq. (9) as

$$\theta^2 = \langle \boldsymbol{\theta}, \boldsymbol{\theta} \rangle = \frac{1}{2}\boldsymbol{\Theta} : \boldsymbol{\Theta} = \frac{1}{2}\mathrm{Tr}(\boldsymbol{\Theta}^2). \tag{10}$$

Noting that $\boldsymbol{n}_\theta \times \boldsymbol{V}_i = (\frac{1}{\theta})\boldsymbol{\Theta}(\theta)\boldsymbol{V}_i$ and using the MacLaurin expansion of $\sin\theta$ and $\cos\theta$ (refer Eq. (29) in Argyris [25]), we get

$$\boldsymbol{Q}(\boldsymbol{\theta}) = \boldsymbol{I}_3 + \frac{\sin\theta}{\theta}\ \boldsymbol{\Theta} + \frac{(1-\cos\theta)}{\theta^2}\boldsymbol{\Theta}^2 = \sum_{i=0}^{n}\frac{\boldsymbol{\Theta}^i}{i!} = e^{\boldsymbol{\Theta}}; \tag{11a}$$

$$\boldsymbol{Q}^T(\boldsymbol{\theta}) = \boldsymbol{I}_3 - \frac{\sin\theta}{\theta}\ \boldsymbol{\Theta} + \frac{(1-\cos\theta)}{\theta^2}\boldsymbol{\Theta}^2 = e^{-\boldsymbol{\Theta}}. \tag{11b}$$

Here, $\boldsymbol{\Theta}^0 = \boldsymbol{I}_3$. Subtracting Eq. (11b) from (11a), we obtain the associated skew-symmetric matrix $\boldsymbol{\Theta}$ as

$$\boldsymbol{\Theta} = \frac{\theta}{2\sin\theta}\left(\boldsymbol{Q} - \boldsymbol{Q}^T\right). \tag{12}$$

Taking trace of $\boldsymbol{Q}$ in Eq. (11a) and using the result in Eq. (10), we get another important relation:

$$\cos\theta = \frac{\mathrm{Tr}(\boldsymbol{Q}) - 1}{2}. \tag{13}$$

It is a known fact that the exponential map is a homeomorphism in the neighborhood of Identity element $\boldsymbol{I}_3 \in SO(3)$ such that $\theta \in [0, \pi)$. That implies the existence of an inverse of exponential map (the logarithm) in the neighborhood of $\boldsymbol{I}_3$ such that

$$\log(\boldsymbol{Q}(\boldsymbol{\theta})) = \log(e^{\boldsymbol{\Theta}}) = \boldsymbol{\Theta} \in so(3). \tag{14}$$

Using the above result along with Eqs. (12) and (13), we get

$$\log(\mathbf{Q}(\boldsymbol{\theta})) = \frac{\theta}{2\sin\theta}\left(\mathbf{Q} - \mathbf{Q}^T\right). \tag{15}$$

We define the norm of logarithm map as the Euclidean norm of the associated rotation vector, such that

$$\|\log(\mathbf{Q}(\boldsymbol{\theta}))\| = \theta = \sqrt{\frac{1}{2}\mathrm{Tr}(\boldsymbol{\Theta}^2)}. \tag{16}$$

Section 3.2.2 discusses local homeomorphism of exponential maps.

3.2.1.2. Unit quaternions. Another approach to capture finite rotations is by using unit quaternions. In general, a quaternion is a 4-tuple $q = q_0 + q_1 i + q_2 j + q_3 k$, where $q_i \in \mathbb{R}$, such that,

$$\begin{aligned} &i^2 = j^2 = k^2 = ijk = -1;\\ &ij = k, ji = -k;\\ &jk = i, kj = -i;\\ &ki = j, ik = -j. \end{aligned} \tag{17}$$

The first of the equations mentioned above has a special significance in the history of mathematics (refer to [26]). The relationship between a complex number and plane geometry inspired *William Rowan Hamilton* to find a higher dimensional number that can be associated with 3D geometry. Hamilton realized need of 4-tuple (not a triplet) to establish a 4D algebra that can be related to 3D geometry, that he called *quaternions*.

The multiplication between two quaternion (called Hamilton product) can be carried in a way similar to the complex numbers using the properties in Eq. (17). Unlike complex numbers, the multiplication of quaternion is non-commutative. The conjugate, norm and inverse of a quaternion are defined as

$$\begin{aligned} &\text{conjugate}: \quad q^* = q_0 - q_1 i - q_2 j - q_3 k;\\ &\text{norm}: \quad \|q\| = \sqrt{qq^*} = \sqrt{q_0^2 + q_1^2 + q_2^2 + q_3^2};\\ &\text{inverse}: \quad q^{-1} = \tfrac{q^*}{\|q\|^2}. \end{aligned} \tag{18}$$

To establish the relationship between a quaternion and 3D geometry, Hamilton suggested considering quaternion to be consisting of a *scalar* and a *vector* (the terms that he proposed), such that $q = (q_0, \boldsymbol{q})$. For two quaternion $q = (q_0, \boldsymbol{q})$ and $a = (a_0, \boldsymbol{a})$, the quaternion sum, Hamilton product, conjugate and norm is then given by:

$$\begin{aligned} &q + a = (q_0 + a_0, \boldsymbol{q} + \boldsymbol{a});\\ &qa = (q_0 a_0 - \langle \boldsymbol{q}, \boldsymbol{a}\rangle, q_0\boldsymbol{a} + a_0\boldsymbol{q} + \boldsymbol{q}\times\boldsymbol{a});\\ &q^* = (q_0, -\boldsymbol{q});\\ &\|q\| = \sqrt{q_0^2 + \langle \boldsymbol{q}, \boldsymbol{q}\rangle}. \end{aligned} \tag{19}$$

We can consider a vector $\boldsymbol{V}_\mathrm{i}$ as a pure quaternion $V_\mathrm{initial} = (0, \boldsymbol{V}_\mathrm{i})$. A unit quaternion $q_\mathrm{u} = (q_0, \boldsymbol{q})$ with $\|q_\mathrm{u}\| = 1$ can be used to rotate vector $\boldsymbol{V}_\mathrm{i}$ to $\boldsymbol{V}_\mathrm{f}$ (with the associated pure quaternion $V_\mathrm{final} = (0, \boldsymbol{V}_\mathrm{f})$), such that

$$\begin{aligned} &V_\mathrm{final} = q_\mathrm{u} V_\mathrm{initial} q_\mathrm{u}^* = (0, \mathbf{Q}(q_\mathrm{u})\boldsymbol{V}_\mathrm{i});\\ &\boldsymbol{V}_\mathrm{f} = \mathbf{Q}(q_\mathrm{u})\boldsymbol{V}_\mathrm{i}. \end{aligned} \tag{20}$$

The rotation tensor $\mathbf{Q}$ can be parametrized by a unit quaternion q_u. If $\boldsymbol{V}_\mathrm{i} = V_{ij}\boldsymbol{E}_j$ and $\boldsymbol{q} = q_i\boldsymbol{E}_i$, then using Eq. (20), we get

$$[\mathbf{Q}(q_\mathrm{u})]_{\boldsymbol{E}_i\otimes\boldsymbol{E}_j} = 2\begin{bmatrix} q_0^2 + q_1^2 - 0.5 & q_1q_2 - q_0q_3 & q_0q_2 + q_1q_3\\ q_0q_3 + q_1q_2 & q_0^2 + q_2^2 - 0.5 & q_2q_3 - q_0q_1\\ q_1q_3 - q_0q_2 & q_0q_1 + q_2q_3 & q_0^2 + q_3^2 - 0.5 \end{bmatrix}. \tag{21}$$

We can parametrize the unit quaternion using the rotation vector $\boldsymbol{\theta}$. Notice from Eq. (21) that the $\mathrm{Tr}(\mathbf{Q}(q_\mathrm{u})) = 4q_0^2 - 1$. A trace being an invariant of a tensor implies (from Eq. (13)) that

$$\begin{aligned} &4q_0^2 - 1 = 2\cos\theta + 1;\\ &q_0 = \sqrt{\tfrac{\cos\theta+1}{2}}. \end{aligned} \tag{22}$$

Thus, there exist two possible and equivalent q_u leading towards same rotation. The q_u with $q_0 > 0$ implies $0 < \theta \leqslant \pi$ about the axis $\boldsymbol{n}_\theta$ and the one with $q_0 < 0$ represents rotation about the axis $-\boldsymbol{n}_\theta$ with the magnitude $2\pi - \theta$, representing same rotation. We call this property as the *equivalence of the unit quaternion and its negative* or *double cover*.

Lets consider $q_0 = \cos\left(\frac{\theta}{2}\right)$. The unity quaternion constraint implies

$$q_\mathrm{u}(\boldsymbol{\theta}) = \left(\cos\left(\frac{\theta}{2}\right), \sin\left(\frac{\theta}{2}\right)\boldsymbol{n}_\theta\right). \tag{23}$$

This representation, sometimes called as rotation vector representation, satisfies the unit quaternion constraint and is same as the Rodrigues rotation.

The *equivalence of the unit quaternion and its negative* in representing rotation was exploited by Klumpp [27] to extract the quaternion from the component of rotation tensor without any singularity. Spurrier [28] recognized the Klumpp's algorithm to be sensitive to numerical imprecision and proposed a modified algorithm, now popularly known as *Spurrier's algorithm*.

The primary disadvantage of representing the rotation using Euler angle formulation is its dependence on the sequence of angles considered and singularities arising due to gimbal lock. Unit quaternion approach completely gets rid of this singularity but is subjected to the unit quaternion constraint. There is plenty of excellent literature to which one may refer for further understanding of rotations (for example, [25,29–31]). The work by Diebel [31] serves as an excellent resource that describes all these approaches and establishes relationships to obtain one form from the other.

3.2.2. On many-to-one nature and local homeomorphism of exponential map

As discussed in Section 3.2.1, the exponential map is a mapping from Lie algebra $so(3)$ to Lie group $SO(3)$. However, the exponential map is not bijective. For a given $\boldsymbol{\Theta} \in so(3)$, there is a unique $\mathbf{Q}(\boldsymbol{\theta}) = e^{\boldsymbol{\Theta}} \in SO(3)$ (thus surjective), however, for a given $\mathbf{Q}(\boldsymbol{\theta}) = e^{\boldsymbol{\Theta}} \in SO(3)$, there are many possible $\boldsymbol{\Theta} \in so(3)$ (hence not injective). For example for $\boldsymbol{\theta}_1 = \theta\boldsymbol{n}_\theta$ and $\boldsymbol{\theta}_2 = (\theta + 2n\pi)\boldsymbol{n}_\theta$ with n being an integer, $\mathbf{Q}(\boldsymbol{\theta}_1) = \mathbf{Q}(\boldsymbol{\theta}_2)$. However, if we restrict $\theta \in [0, \pi)$, we obtain a local homeomorphism in the exponential map as explained below.

Let us start our discussion by restricting $\theta \in [-\pi, \pi)$. For this case every rotation tensor identifies a unit vector as $\pm\boldsymbol{n}_\theta$ (unique up to a multiple of ± 1) except at $\theta = -\pi$, in which case $\boldsymbol{n}_\theta$ is unique. Thus, the rotation angle and unit vector combination $(\theta, \boldsymbol{n}_\theta)$ and $(-\theta, -\boldsymbol{n}_\theta)$ defines same rotation vector. This fact looks trivial because $\boldsymbol{\theta} = \theta\boldsymbol{n}_\theta$, however, it forbids us to uniquely define a unit rotation vector $\boldsymbol{n}_\theta$.

To uniquely define the unit rotation vector $\boldsymbol{n}_\theta$, we restrict θ to positive value $\theta \in [0, \pi)$. At $\theta = 0$, the unit vector $\boldsymbol{n}_\theta$ can be any arbitrary vector but $\boldsymbol{\theta} = \boldsymbol{0}$ and the corresponding rotation tensor is $\mathbf{Q} = \boldsymbol{I}_3$. At $\theta = \pi$, there are two possible unit vectors $\pm\boldsymbol{n}_\theta$ (thus, the map is not homeomorphic for $\theta = \pi$). Thus, the exponential map is local homeomorphism in the neighborhood of $\boldsymbol{I}_3$ such that $\theta \in [0, \pi)$.

From Eq. (13), $\mathrm{Tr}(\mathbf{Q}) = -1$ at $\theta = \pi$. Therefore, the logarithm map is a well-defined continuous map if $\mathrm{Tr}(\mathbf{Q}) \neq -1$ and $\theta \in [0, \pi)$. Eq. (15) can be used to obtain logarithm of rotation tensor (the associates spin matrix), however, as θ approaches 0 and π radians, Eq. (15) becomes unstable as $\sin\theta$ vanishes. Spurrier's algorithm [28] can be used to extract the quaternions and the associated rotation vector. Spurrier's algorithm gives $\theta \in [0, \pi]$ and

restricts quaternion component $q_0 \geqslant 0$. However, at $q_0 = 0$ or equivalently $\theta = \pi$, there are two possible unit vectors. The quaternions are related to the rotation vector $\boldsymbol{\theta} = \theta \boldsymbol{n}_\theta$ by the following relationships:

$$\begin{aligned} &\theta = 2\arcsin\left(\sqrt{q_1^2+q_2^2+q_3^2}\right) = 2\arccos(q_0);\\ &n_{\theta i} = \frac{q_i}{\sqrt{q_1^2+q_2^2+q_3^2}}. \end{aligned} \tag{24}$$

3.2.3. Rotation of a triad: rotation matrix

The entity $\boldsymbol{Q}$ discussed in previous section, transforms one vector to another. Therefore, it is a tensor. However, consider a properly orthonormal triad $\{\boldsymbol{d}_i\}$ such that $\boldsymbol{d}_i = \boldsymbol{Q}\boldsymbol{E}_i$. We can then obtain *direction cosine matrix* $\mathfrak{R}$ such that, $[d_1, d_2, d_3]^T = \mathfrak{R}.[E_1, E_2, E_3]^T$. The component of matrix $\mathfrak{R}_{ij} = \langle d_i, E_j\rangle = Q_{ji}$. Here, Q_{ji} represents $\boldsymbol{E}_j \otimes \boldsymbol{E}_i$ component of the rotation tensor $\boldsymbol{Q}$. It can be observed that $\mathfrak{R} = [Q]^T_{E_i\otimes E_j}$. Notice that $\mathfrak{R}$ is a matrix whereas $\boldsymbol{Q}$ is a tensor.

3.3. Construction of MAF and MF

In this section, we construct these frames by carrying finite rotations of the fixed orthogonal triad $\{\boldsymbol{E}_i\}$ using Euler angle approach. We use the following notations: $\cos\theta = c_\theta$ and $\sin\theta = s_\theta$, for any angle θ.

3.3.1. Special material adapted frame: SMAF

Consider a regular and at least C^2 continuous curve $\boldsymbol{\varphi}(\xi_1)$. Let $\boldsymbol{Q}_s \in SO(3)$ be the rotation tensor that generates SMAF consisting of orthonormal triad $\{\boldsymbol{T}, \boldsymbol{Y}_s, \boldsymbol{P}_s\}$, such that $\langle \boldsymbol{P}_s, \boldsymbol{E}_2\rangle = 0$. This can be obtained by first rotating the frame $\{\boldsymbol{E}_i\}$ about $\boldsymbol{E}_2$ by an angle ϕ_y (yaw angle) and then rotating about the updated $\boldsymbol{E}_3$ by an angle ϕ_p (pitch angle). Thus, if, $\boldsymbol{Q}_s = \boldsymbol{T}\otimes\boldsymbol{E}_1 + \boldsymbol{Y}_s\otimes\boldsymbol{E}_2 + \boldsymbol{P}_s\otimes\boldsymbol{E}_3$, then,

$$\begin{bmatrix}\boldsymbol{T}\\ \boldsymbol{Y}_s\\ \boldsymbol{P}_s\end{bmatrix} = \overbrace{\begin{bmatrix} c_{\phi_p}c_{\phi_y} & s_{\phi_p} & -c_{\phi_p}s_{\phi_y}\\ -s_{\phi_p}c_{\phi_y} & c_{\phi_p} & s_{\phi_p}s_{\phi_y}\\ s_{\phi_y} & 0 & c_{\phi_y}\end{bmatrix}}^{[\boldsymbol{Q}_s]^T_{\boldsymbol{E}_i\otimes\boldsymbol{E}_j}} \begin{bmatrix}\boldsymbol{E}_1\\ \boldsymbol{E}_2\\ \boldsymbol{E}_3\end{bmatrix}. \tag{25}$$

Here, $\boldsymbol{Y}_s$ and $\boldsymbol{P}_s$ represent the yaw and pitch axis respectively.

The fact that $\langle \boldsymbol{P}_s(\xi_1), \boldsymbol{E}_2\rangle = 0$ or $\boldsymbol{P}_s(\xi_1)$ lies in $(\boldsymbol{E}_1 - \boldsymbol{E}_3)$ plane is advantageous in practical standpoint. This is because $\boldsymbol{P}_s(\xi_1)$ acts as a reference vector in the normal plane with respect to which, the torsion angle or the roll angle and the shear angles can be defined to obtain GMAF and MF. Note that we can define another special case in which only one angle is non-zero (either pitch or yaw angle). But that would define a curve in 2D plane, hence not desirable for spatial curves.

3.3.2. General material adapted frame: GMAF

Rotating SMAF about the tangent vector by an angle ϕ_r (roll angle) gives us GMAF consisting of orthonormal triad $\{\boldsymbol{T}, \boldsymbol{Y}_g, \boldsymbol{P}_g\}$, obtained by finite rotation of $\{\boldsymbol{E}_i\}$ by the rotation tensor $\boldsymbol{Q}_g$, such that $\boldsymbol{Q}_g = \boldsymbol{T}\otimes\boldsymbol{E}_1 + \boldsymbol{Y}_g\otimes\boldsymbol{E}_2 + \boldsymbol{P}_g\otimes\boldsymbol{E}_3$. Thus,

$$\begin{bmatrix}\boldsymbol{T}\\ \boldsymbol{Y}_g\\ \boldsymbol{P}_g\end{bmatrix} = \overbrace{\begin{bmatrix} c_{\phi_p}c_{\phi_y} & s_{\phi_p} & -c_{\phi_p}s_{\phi_y}\\ -c_{\phi_r}c_{\phi_y}s_{\phi_p} + s_{\phi_r}s_{\phi_y} & c_{\phi_p}c_{\phi_r} & c_{\phi_y}s_{\phi_r} + c_{\phi_r}s_{\phi_p}s_{\phi_y}\\ c_{\phi_y}s_{\phi_p}s_{\phi_r} + c_{\phi_r}s_{\phi_y} & -c_{\phi_p}s_{\phi_r} & c_{\phi_r}c_{\phi_y} - s_{\phi_p}s_{\phi_r}s_{\phi_y}\end{bmatrix}}^{[\boldsymbol{Q}_g]^T_{\boldsymbol{E}_i\otimes\boldsymbol{E}_j}} \begin{bmatrix}\boldsymbol{E}_1\\ \boldsymbol{E}_2\\ \boldsymbol{E}_3\end{bmatrix}. \tag{26}$$

This sequence of rotations falls under Tiat-Bryan intrinsic rotation with the sequence yaw first, pitch second and roll third.

3.3.3. Material frames: MF

As discussed in Section 3.1, we might encounter a situation in which the plane of interest need not be normal to the curve. Consider a general orthogonal triad $\{\boldsymbol{d}_i\}$ such that the vector $\boldsymbol{d}_1$ is not along the tangent vector of the curve $\boldsymbol{T}$ and the vectors $\{\boldsymbol{d}_2 - \boldsymbol{d}_3\}$ spans a plane normal to $\boldsymbol{d}_1$. For instance, a cross-section of a beam subjected to shear is not normal to the tangent vector or a rigid swarm of drones need not be perpendicular to the direction of motion. In such instances, MF are desirable.

Consider a general orthonormal frame $\{\boldsymbol{d}_i\}$ with its origin at some point on the curve. It can be obtained from finite rotation of the frame $\{\boldsymbol{E}_i\}$ such that $\boldsymbol{d}_i = \boldsymbol{Q}_m\boldsymbol{E}_i$ or from any other triad, say SMAF using the rotation tensor $\boldsymbol{Q}_{ms}$ such that,

$$\begin{aligned} &\boldsymbol{Q}_m = \sum_{i=1}^{3}\boldsymbol{d}_i\otimes\boldsymbol{E}_i;\\ &\boldsymbol{Q}_{ms} = \boldsymbol{d}_1\otimes\boldsymbol{T} + \boldsymbol{d}_2\otimes\boldsymbol{Y}_s + \boldsymbol{d}_3\otimes\boldsymbol{P}_s;\\ &\boldsymbol{Q}_m = \boldsymbol{Q}_{ms}\boldsymbol{Q}_s. \end{aligned} \tag{27}$$

4. Curvature of an evolving frame

4.1. Curvatures of a general material frame

Let us consider the material frame $\{\boldsymbol{d}_i\}$. The frame is a function of the quantity parameterizing the curve under consideration. The choice of parameter is problem-dependent. For instance, the frame attached to a UAV is evolving with *time*. Similarly, a frame representing the orientation of a cross-section of a beam varies along the *arclength* of the deformed beam or the frame attached at a fixed cross-section of a cable changes with *time* when the cable undergoes dynamic deformation. The change of directors with respect to the parameter gives local information about deviation of the configuration of system at a point. For instance, the curvature $\overline{\kappa}$ of Frenet frame gives the deviation of the curve from its tangent vector at the given arclength.

The derivative of the director triad $\{\boldsymbol{d}_i\}$ with respect to the arclength parameter ξ_1 is obtained using the Eq. (27) as

$$\boldsymbol{d}_{i,\xi_1} = \boldsymbol{Q}_{m,\xi_1}\boldsymbol{E}_i = \boldsymbol{Q}_{m,\xi_1}\boldsymbol{Q}_m^T\boldsymbol{d}_i = \boldsymbol{K}\boldsymbol{d}_i = \boldsymbol{\kappa}\times\boldsymbol{d}_i. \tag{28}$$

Since $\boldsymbol{Q}_m \in SO(3)$, it can be proved that $\boldsymbol{K} = \boldsymbol{Q}_{m,\xi_1}\boldsymbol{Q}_m^T$ is anti-symmetric with corresponding axial vector $\boldsymbol{\kappa}$. Here, $\boldsymbol{\kappa} = \kappa_i\boldsymbol{E}_i = \overline{\kappa}_i\boldsymbol{d}_i$, represents the Darboux vector of the frame when parameterized by the arclength ξ_1. Note that the overline on the components $\overline{\kappa}_i$ represents the component of the Darboux vector in the MF. In matrix form,

$$\begin{bmatrix}\boldsymbol{d}_{1,\xi_1}\\ \boldsymbol{d}_{2,\xi_1}\\ \boldsymbol{d}_{3,\xi_1}\end{bmatrix} = \overbrace{\begin{bmatrix} 0 & \overline{\kappa}_3 & -\overline{\kappa}_2\\ -\overline{\kappa}_3 & 0 & \overline{\kappa}_1\\ \overline{\kappa}_2 & -\overline{\kappa}_1 & 0\end{bmatrix}}^{\boldsymbol{K}^T} \begin{bmatrix}\boldsymbol{d}_1\\ \boldsymbol{d}_2\\ \boldsymbol{d}_3\end{bmatrix}. \tag{29}$$

4.1.1. Curvature terms of Frenet frame

The fact that the tangent vector $\boldsymbol{T}(\xi_1)$ depends on the pitch ϕ_p and yaw angle ϕ_y, enables us to represent the Frenet frame in terms of these functions. With the rotation about $\boldsymbol{E}_2$ first followed by the rotation about the updated $\boldsymbol{E}_3$, and using the results discussed in Section 2.1, the following results can be obtained

$$\boldsymbol{\varphi}(\xi_1) = \boldsymbol{\varphi}(0) + \int_0^{\xi_1}\boldsymbol{T}(s)\mathrm{d}s; \tag{30a}$$

$$\overline{\kappa} = \sqrt{\phi_{p,\xi_1}^2 + \phi_{y,\xi_1}^2 c_{\phi_p}^2}; \tag{30b}$$

$$\overline{\tau} = \left(\frac{1}{\overline{\kappa}^2}\right)\left(\phi_{y,\xi_1}\left(2s_{\phi_p}\phi_{p,\xi_1}^2 + c_{\phi_p}\left(c_{\phi_p}s_{\phi_p}\phi_{y,\xi_1}^2 + \phi_{p,\xi_1\xi_1}\right)\right) - c_{\phi_p}\phi_{p,\xi_1}\phi_{y,\xi_1\xi_1}\right); \tag{30c}$$

$$[\mathbf{Q}_{\mathrm{f}}]^T_{\boldsymbol{E}_i\otimes\boldsymbol{E}_j} = \left(\frac{1}{\overline{\kappa}}\right)\begin{bmatrix} \overline{\kappa}c_{\phi_p}c_{\phi_y} & \overline{\kappa}s_{\phi_p} & -\overline{\kappa}c_{\phi_p}s_{\phi_y} \\ -c_{\phi_y}s_{\phi_p}\phi_{p,\xi_1} - c_{\phi_p}s_{\phi_y}\phi_{y,\xi_1} & c_{\phi_p}\phi_{p,\xi_1} & s_{\phi_p}s_{\phi_y}\phi_{p,\xi_1} - c_{\phi_p}c_{\phi_y}\phi_{y,\xi_1} \\ s_{\phi_y}\phi_{p,\xi_1} - c_{\phi_p}c_{\phi_y}s_{\phi_p}\phi_{y,\xi_1} & c_{\phi_p}^2\phi_{y,\xi_1} & c_{\phi_y}\phi_{p,\xi_1} + c_{\phi_p}s_{\phi_p}s_{\phi_y}\phi_{y,\xi_1} \end{bmatrix}. \tag{30d}$$

4.1.2. Curvature terms of SMAF and GMAF

From Eqs. (25) and (28), we arrive at the Darboux vector for the SMAF $\boldsymbol{\kappa}_{\mathrm{s}} = \overline{\kappa}_{\mathrm{s}1}\boldsymbol{T} + \overline{\kappa}_{\mathrm{s}2}\boldsymbol{Y}_{\mathrm{s}} + \overline{\kappa}_{\mathrm{s}3}\boldsymbol{P}_{\mathrm{s}}$ such that,

$$\overline{\kappa}_{\mathrm{s}1} = \phi_{y,\xi_1}s_{\phi_p}; \quad \overline{\kappa}_{\mathrm{s}2} = \phi_{y,\xi_1}c_{\phi_p}; \quad \overline{\kappa}_{\mathrm{s}3} = \phi_{p,\xi_1}. \tag{31a}$$

$$\langle \boldsymbol{\kappa}_{\mathrm{s}}, \boldsymbol{\kappa}_{\mathrm{s}}\rangle = \phi_{p,\xi_1}^2 + \phi_{y,\xi_1}^2; \tag{31b}$$

$$\overline{\kappa}^2 = \overline{\kappa}_{\mathrm{s}2}^2 + \overline{\kappa}_{\mathrm{s}3}^2. \tag{31c}$$

Similarly, from Eqs. (26) and (29), we arrive at the Darboux vector for the GMAF, $\boldsymbol{\kappa}_{\mathrm{g}} = \overline{\kappa}_{\mathrm{g}1}\boldsymbol{T} + \overline{\kappa}_{\mathrm{g}2}\boldsymbol{Y}_{\mathrm{g}} + \overline{\kappa}_{\mathrm{g}3}\boldsymbol{P}_{\mathrm{g}}$ such that,

$$\overline{\kappa}_{\mathrm{g}1} = \phi_{r,\xi_1} + \phi_{y,\xi_1}s_{\phi_p} = \phi_{r,\xi_1} + \overline{\kappa}_{\mathrm{s}1}; \tag{32a}$$

$$\overline{\kappa}_{\mathrm{g}2} = \phi_{y,\xi_1}c_{\phi_p}c_{\phi_r} + s_{\phi_r}\phi_{p,\xi_1} = \overline{\kappa}_{\mathrm{s}2}c_{\phi_r} + \overline{\kappa}_{\mathrm{s}3}s_{\phi_r}; \tag{32b}$$

$$\overline{\kappa}_{\mathrm{g}3} = c_{\phi_r}\phi_{p,\xi_1} - c_{\phi_p}s_{\phi_r}\phi_{y,\xi_1} = -\overline{\kappa}_{\mathrm{s}2}s_{\phi_r} + \overline{\kappa}_{\mathrm{s}3}c_{\phi_r}; \tag{32c}$$

$$\langle \boldsymbol{\kappa}_{\mathrm{g}}, \boldsymbol{\kappa}_{\mathrm{g}}\rangle = \left(\phi_{p,\xi_1}^2 + \phi_{y,\xi_1}^2 + \phi_{r,\xi_1}^2\right) + 2s_{\phi_p}\phi_{r,\xi_1}\phi_{y,\xi_1}. \tag{32d}$$

It is interesting to note from above relations that

$$\begin{bmatrix} \overline{\kappa}_{\mathrm{g}1} \\ \overline{\kappa}_{\mathrm{g}2} \\ \overline{\kappa}_{\mathrm{g}3} \end{bmatrix} = \begin{bmatrix} 1 & 0 & 0 \\ 0 & c_{\phi_r} & s_{\phi_r} \\ 0 & -s_{\phi_r} & c_{\phi_r} \end{bmatrix}\begin{bmatrix} \overline{\kappa}_{\mathrm{s}1} \\ \overline{\kappa}_{\mathrm{s}2} \\ \overline{\kappa}_{\mathrm{s}3} \end{bmatrix} + \begin{bmatrix} \phi_{r,\xi_1} \\ 0 \\ 0 \end{bmatrix}. \tag{33}$$

The curvatures in terms of quaternions and Rodrigues parameters are presented in the Appendix A.1.

4.2. RPAF and Frenet frame as GMAF

The RPAF can be considered as GMAF with $\phi_r = \rho_{\mathrm{b}}$ representing the rotation of the normal vectors $\boldsymbol{N}_1$ and $\boldsymbol{N}_2$ from the vector $\boldsymbol{Y}_{\mathrm{s}}$ and $\boldsymbol{P}_{\mathrm{s}}$ respectively, in a constrained fashion. It is clear from Eqs. (6) and (29) that the constraint over RPAF is $\overline{\kappa}_{\mathrm{g}3} = 0$. With this constraint in mind, we can obtain the roll angle field $\rho_{\mathrm{b}}(\xi_1)$ for the RPAF by using Eq. (32a). We have

$$\rho_{\mathrm{b}}(\xi_1) = \rho_{\mathrm{b}}(0) - \int_0^{\xi_1}\overline{\kappa}_{\mathrm{s}1}(k)\mathrm{d}k. \tag{34}$$

Fixing the value of $\rho_{\mathrm{b}}(0)$ provides uniqueness to the RPAF. From Eqs. (32b) and (32c), we can arrive at the expression of the normal development (or curvatures) of RPAF in terms of the Euler angles associated with the GMAF as

$$\overline{\kappa}_1 = -\overline{\kappa}_{\mathrm{g}2}|_{(\phi_r=\rho_{\mathrm{b}})} = -\overline{\kappa}_{\mathrm{s}3}s_{\rho_{\mathrm{b}}} - \overline{\kappa}_{\mathrm{s}2}c_{\rho_{\mathrm{b}}}; \tag{35a}$$

$$\overline{\kappa}_2 = \overline{\kappa}_{\mathrm{g}3}|_{(\phi_r=\rho_{\mathrm{b}})} = \overline{\kappa}_{\mathrm{s}3}c_{\rho_{\mathrm{b}}} + \overline{\kappa}_{\mathrm{s}2}s_{\rho_{\mathrm{b}}}. \tag{35b}$$

Substituting for $\overline{\kappa}_1$ and $\overline{\kappa}_2$ from the results obtained in Eqs. (35a) and (35b) into the Eq. (7a) yields the result in Eq. (31c). Using Eqs. (35a) and (35b) along with the result in (7c), we arrive at an important relationship between the angle ρ_{b} and η, thus enabling us to express Frenet frame as a GMAF (refer Fig. 2).

$$\tan\rho_{\mathrm{b}} = -\left(\frac{\overline{\kappa}_{\mathrm{s}2} + \overline{\kappa}_{\mathrm{s}3}\tan\eta}{\overline{\kappa}_{\mathrm{s}3} + \overline{\kappa}_{\mathrm{s}2}\tan\eta}\right). \tag{36}$$

We can independently arrive at the angle $(\phi_r = \rho_{\mathrm{f}})$ subtended by the vectors $\boldsymbol{N}$ and $\boldsymbol{B}$ with $\boldsymbol{Y}_{\mathrm{s}}$ and $\boldsymbol{P}_{\mathrm{s}}$ respectively by imposing a constraint $\overline{\kappa}_{\mathrm{g}2} = 0$ on GMAF such that,

$$\tan\rho_{\mathrm{f}} = -\frac{\overline{\kappa}_{\mathrm{s}2}}{\overline{\kappa}_{\mathrm{s}3}} = \tan(\eta + \rho_{\mathrm{b}}). \tag{37}$$

We note that the results obtained in Eqs. (36) and (37) are consistent.

Fig. 3 shows a curve with the point of inflection marked by a dot, the red vectors representing the tangent vector field and the circles representing the normal plane to the curve. In Fig. 3a, the solid green and blue arrows represent $\boldsymbol{Y}_{\mathrm{s}}$ and $\boldsymbol{P}_{\mathrm{s}}$ field, whereas the dotted green and blue vectors stand for $\boldsymbol{N}_1$ and $\boldsymbol{N}_2$ respectively. Similarly, the green and blue vectors in Fig. 3b show $\boldsymbol{N}$ and $\boldsymbol{B}$ respectively. Fig. 3a and b shows that the SMAF and RPAF (obtained using Eq. (34) and setting $\rho_{\mathrm{b}}(0) = 0$) are continuous whereas the Frenet frame is not uniquely defined at the point of inflection and the normal vector (binormal vector as well) abruptly changes its orientations at the inflection point.

4.3. Linear and angular velocity

A regular C^r continuous curve $\boldsymbol{\varphi}(\xi_1)$ parametrized by the arclength ξ_1 can be re-parametrized by another variable t (say time) such that $\xi_1 = \xi_1(t)$ is at least C^1 continuous and $\frac{\mathrm{d}\xi_1}{\mathrm{d}t} \neq 0$. We define linear velocity of the curve as,

$$\begin{aligned} \boldsymbol{\varphi}_{,t} &= \frac{\partial\boldsymbol{\varphi}}{\partial t} = \frac{\partial\boldsymbol{\varphi}}{\partial\xi_1}\frac{\mathrm{d}\xi_1}{\mathrm{d}t} = \frac{\mathrm{d}\xi_1}{\mathrm{d}t}\boldsymbol{T} = v(t)\boldsymbol{T}; \\ \boldsymbol{\varphi}_{,t} &= \overline{v}_i\boldsymbol{d}_i = v(t)(\overline{t}_i\boldsymbol{d}_i) \ \text{ where } \ \boldsymbol{T} = \overline{t}_i\boldsymbol{d}_i. \end{aligned} \tag{38}$$

The scalar $v(t) = \frac{\mathrm{d}\xi_1}{\mathrm{d}t} = \sqrt{\overline{v}_1^2 + \overline{v}_2^2 + \overline{v}_3^2}$ gives the magnitude of linear velocity vector at time t. The angular velocity vector $\boldsymbol{\omega}$ is related to the evolution of the frame when the curve is parametrized by time.

Let us consider the derivative of the director triad $\{\boldsymbol{d}_i(t)\}$ with respect to time t. From Eq. (27), we have,

$$\boldsymbol{d}_{i,t} = \mathbf{Q}_{\mathrm{m},t}\boldsymbol{E}_i = \mathbf{Q}_{\mathrm{m},t}\mathbf{Q}_{\mathrm{m}}^T\boldsymbol{d}_i = \boldsymbol{W}(t)\boldsymbol{d}_i = \boldsymbol{\omega}(t)\times\boldsymbol{d}_i(t). \tag{39}$$

The fact that $\boldsymbol{K} = \mathbf{Q}_{\mathrm{m},\xi_1}\mathbf{Q}_{\mathrm{m}}^T$ implies that $\boldsymbol{W}(t) = v(t)\boldsymbol{K}(\xi_1(t))$ or $\boldsymbol{\omega}(t) = v(t)\boldsymbol{\kappa}(\xi_1(t))$. Thus,

$$\begin{bmatrix} \boldsymbol{d}_{1,t} \\ \boldsymbol{d}_{2,t} \\ \boldsymbol{d}_{3,t} \end{bmatrix} = v(t)\begin{bmatrix} 0 & \overline{\kappa}_3(\xi_1(t)) & -\overline{\kappa}_2(\xi_1(t)) \\ -\overline{\kappa}_3(\xi_1(t)) & 0 & \overline{\kappa}_1(\xi_1(t)) \\ \overline{\kappa}_2(\xi_1(t)) & -\overline{\kappa}_1(\xi_1(t)) & 0 \end{bmatrix}\begin{bmatrix} \boldsymbol{d}_1 \\ \boldsymbol{d}_2 \\ \boldsymbol{d}_3 \end{bmatrix};$$

$$\begin{bmatrix} \boldsymbol{d}_{1,t} \\ \boldsymbol{d}_{2,t} \\ \boldsymbol{d}_{3,t} \end{bmatrix} = \begin{bmatrix} 0 & \overline{\omega}_3(t) & -\overline{\omega}_2(t) \\ -\overline{\omega}_3(t) & 0 & \overline{\omega}_1(t) \\ \overline{\omega}_2(t) & -\overline{\omega}_1(t) & 0 \end{bmatrix}\begin{bmatrix} \boldsymbol{d}_1 \\ \boldsymbol{d}_2 \\ \boldsymbol{d}_3 \end{bmatrix}. \tag{40}$$

Note that $\boldsymbol{\omega} = \overline{\omega}_i\boldsymbol{d}_i = \omega_i\boldsymbol{E}_i$ such that $[\omega_1,\omega_2,\omega_3]^T = [\mathbf{Q}_{\mathrm{m}}]_{\boldsymbol{E}_i\otimes\boldsymbol{E}_j}\cdot[\overline{\omega}_1,\overline{\omega}_2,\overline{\omega}_3]^T$.

The results presented so far describes the construction of various frames, their curvatures and their relationship to each other. These results will be used to develop algorithm to estimate a smooth framed curve from limited set of curvature data.

5. Estimating the global state space of single-manifold characterized system using limited number of material curvature and velocity data

5.1. Configuration and state space of single-manifold characterized systems

5.1.1. Tangent space and tangent bundle of the configuration space

Consider a rigid body, the configuration of which is defined by a space curve $\boldsymbol{\varphi}$ and the vector triad field $\{\boldsymbol{d}_i\}$ that defines the orientation of the rigid body under motion. Thus, the configuration

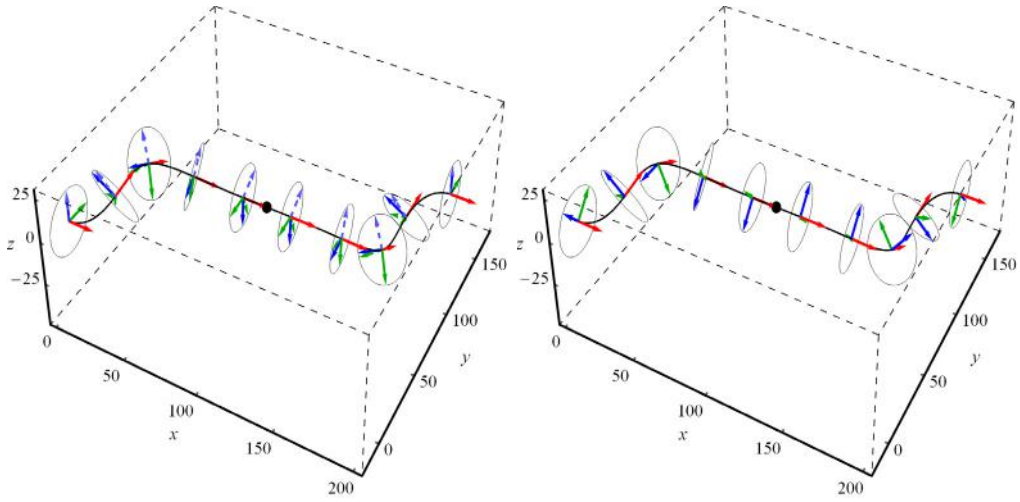

(a) *SMAF and RPAF (dashed arrows)* (b) *Frenet frame*

Fig. 3. Example of a curve with point of inflection (marked by black dot) and the SMAF, RPAF and Frenet frames.

space $\mathfrak{C} := \mathbb{R}^3 \times SO(3) \equiv SE(3)$ defines such systems and is parametrized by a single-parameter (time in case of rigid body motion). Here $SE(3)$ is the *special Euclidean group*, that defines rigid body motion. Thus,

$$\boldsymbol{\Phi}(t) := \{(\boldsymbol{\varphi}(t), \boldsymbol{Q}(t))| \quad \boldsymbol{\varphi} : \mathbb{R}^+ \to \mathbb{R}^3, \quad \boldsymbol{Q} : \mathbb{R}^+ \to SO(3)\} \subset \mathfrak{C}. \tag{41}$$

In the equation above, $\mathbb{R}^+$ represents set of non-negative real number. If $\xi_1(t) \in \mathbb{R}^+$ represents the total distance travel at time $t \in \mathbb{R}^+$, the linear velocity is defined as $\xi_{1,t} = v(t)$.

Consider the curve parametrized by the arclength ξ_1. For any $\boldsymbol{\Phi}(\xi_1) \in \mathfrak{C}$, we define the tangent space $T_{\boldsymbol{\Phi}}\mathfrak{C}$ as,

$$T_{\boldsymbol{\Phi}}\mathfrak{C} := \left\{\left(\boldsymbol{\varphi}_{,\xi_1}, \boldsymbol{Q}_{,\xi_1}\right)| \ \boldsymbol{\varphi}_{,\xi_1} : \mathbb{R}^+ \to \mathbb{R}^3, \ \boldsymbol{Q}_{,\xi_1} = \boldsymbol{K}\boldsymbol{Q} : \mathbb{R}^+ \to T_{\boldsymbol{Q}}SO(3)\right\}. \tag{42}$$

Here, $T_{\boldsymbol{Q}}SO(3)$ refers to the tangent plane of the non-linear manifold $SO(3)$ at $\boldsymbol{Q}$ such that $\boldsymbol{Q}_{,\xi_1} \in T_{\boldsymbol{Q}}SO(3)$. We recall that $\boldsymbol{K} = \boldsymbol{Q}_{,\xi_1}\boldsymbol{Q}^T$ is an antisymmetric matrix with the axial vector $\boldsymbol{\kappa}(\xi_1)$. If the rotation tensor $\boldsymbol{Q}$ is parametrized by the rotation vector $\boldsymbol{\theta} = \theta\boldsymbol{n}_\theta$ as shown in the Section 3.2, then using Eq. (11a) the following relationship is obtained

$$\begin{aligned}\boldsymbol{K} = &\left(\frac{\sin\theta}{\theta}\right)\boldsymbol{\Theta}_{,\xi_1} + \left(\frac{1-\cos\theta}{\theta^2}\right)(\boldsymbol{\Theta}\boldsymbol{\Theta}_{,\xi_1} - \boldsymbol{\Theta}_{,\xi_1}\boldsymbol{\Theta}) \\ &+ \left(\frac{\theta-\sin\theta}{\theta^3}\right)\langle\boldsymbol{\theta}, \boldsymbol{\theta}_{,\xi_1}\rangle\boldsymbol{\Theta}.\end{aligned} \tag{43}$$

In the equation above, $(\boldsymbol{\Theta}\boldsymbol{\Theta}_{,\xi_1} - \boldsymbol{\Theta}_{,\xi_1}\boldsymbol{\Theta}) := [\boldsymbol{\Theta}, \boldsymbol{\Theta}_{,\xi_1}]$ is the Lie bracket of two anti-symmetric matrices. The action of the Lie bracket on any vector $\boldsymbol{p} \in \mathbb{R}^3$ is given by: $[\boldsymbol{\Theta}, \boldsymbol{\Theta}_{,\xi_1}]\boldsymbol{p} = (\boldsymbol{\theta} \times \boldsymbol{\theta}_{,\xi_1}) \times \boldsymbol{p}$. Using Eq. (43) and the definition of Lie bracket, we obtain the corresponding axial vector (the curvature vector) as

$$\begin{aligned}&\boldsymbol{\kappa} = \boldsymbol{T}_\theta\boldsymbol{\theta}_{,\xi_1}; \\ &\boldsymbol{\theta}_{,\xi_1} = \boldsymbol{T}_\theta^{-1}\boldsymbol{\kappa}; \\ &\boldsymbol{T}_\theta = \tfrac{\sin\theta}{\theta}\boldsymbol{I}_3 + \tfrac{1-\cos\theta}{\theta^2}\boldsymbol{\Theta} + \left[\tfrac{\theta-\sin\theta}{\theta^3}\right]\boldsymbol{\theta}\otimes\boldsymbol{\theta}; \\ &\boldsymbol{T}_\theta^{-1} = \tfrac{1}{2}\tfrac{\theta}{\tan\frac{\theta}{2}}\boldsymbol{I}_3 - \tfrac{1}{2}\boldsymbol{\Theta} + \tfrac{1}{\theta^2}\left[1 - \tfrac{1}{2}\tfrac{\theta}{\tan\frac{\theta}{2}}\right]\boldsymbol{\theta}\otimes\boldsymbol{\theta}.\end{aligned} \tag{44}$$

Refer to Ibrahimbegovic [29] for the derivation of $\boldsymbol{T}_\theta^{-1}$. In the above equations, $\boldsymbol{\Theta}$ and $\boldsymbol{\Theta}_{,\xi_1}$ represents the spin matrix associated with the vector $\boldsymbol{\theta}$ and $\boldsymbol{\theta}_{,\xi_1}$ respectively.

Therefore, with slight abuse of notation, we define an abused but equivalent tangent space as,

$$T_{\boldsymbol{\Phi}}\mathfrak{C} \equiv \left\{\tilde{\boldsymbol{\Phi}} = \left(\boldsymbol{\varphi}_{,\xi_1}, \boldsymbol{\kappa}\right)| \quad \boldsymbol{\varphi}_{,\xi_1} : \mathbb{R}^+ \to \mathbb{R}^3, \quad \boldsymbol{\kappa} : \mathbb{R}^+ \to \mathbb{R}^3\right\} \subset \mathbb{R}^3 \times \mathbb{R}^3. \tag{45}$$

A one-to-one correspondence between $\mathbb{R}^3$ and $so(3)$ justifies this abuse of notation. The state space of the problem is defined by the tangent bundle $T\mathfrak{C}$ of the configuration space $\mathfrak{C}$ defined as,

$$T\mathfrak{C} := \{(\boldsymbol{\Phi}, \tilde{\boldsymbol{\Phi}})| \quad \boldsymbol{\Phi} \in \mathfrak{C}, \quad \tilde{\boldsymbol{\Phi}} \in T_{\boldsymbol{\Phi}}\mathfrak{C}\}. \tag{46}$$

From Eqs. (45) and (46) it is clear that the state space is defined by the set $\left(\boldsymbol{\varphi}, \{\boldsymbol{d}_i\}, \boldsymbol{\varphi}_{,\xi_1}, \boldsymbol{\kappa}\right)$.

5.1.2. Material and spatial representation of curvature (or equivalently angular velocity and the associated spin tensor)

We define the quantity $\overline{\boldsymbol{K}} = \boldsymbol{Q}^T\boldsymbol{K}\boldsymbol{Q} \in T_{\boldsymbol{I}_3}SO(3) := so(3)$ obtained by parallel transport of $\boldsymbol{K}\boldsymbol{Q}$ from $T_{\boldsymbol{Q}}SO(3) \to so(3)$. Here, $\boldsymbol{I}_3 = \boldsymbol{E}_i \otimes \boldsymbol{E}_i$ represents the rotation tensor with respect to which the motion is calibrated and is usually taken as identity.

Thus, if $\boldsymbol{Q} = \boldsymbol{d}_i \otimes \boldsymbol{d}_i$, such that $\boldsymbol{d}_i = \boldsymbol{Q}\boldsymbol{E}_i$, then $\boldsymbol{Q}$ represents the finite rotation, whereas $\overline{\boldsymbol{K}}$ represents an infinitesimal rotation with respect to the calibrating frame of reference $\{\boldsymbol{E}_i\}$. Whereas, $\boldsymbol{Q}\overline{\boldsymbol{K}} = \boldsymbol{K}\boldsymbol{Q}$ represents infinitesimal rotation with respect to $\{\boldsymbol{d}_i\}$ frame. In the physical context of rotation, the tangent vector $\boldsymbol{Q}\overline{\boldsymbol{K}}$ and $\boldsymbol{K}\boldsymbol{Q}$ performs an infinitesimal rotation with respect to $\{\boldsymbol{d}_i\}$ frame but the quantity $\boldsymbol{Q}\overline{\boldsymbol{K}}$ is obtained by left translation of the quantity $\overline{\boldsymbol{K}} \in so(3)$ to $\boldsymbol{Q}\overline{\boldsymbol{K}} \in T_{\boldsymbol{Q}}SO(3)$, whereas, $\boldsymbol{K}\boldsymbol{Q}$ represents the superimposition of infinitesimal rotation contributed by $\boldsymbol{K}$ onto the finite rotation contributed by $\boldsymbol{Q}$ (this is also called as right translation of $\boldsymbol{K} \in so(3)$ to the tangent vector $\boldsymbol{K}\boldsymbol{Q} \in T_{\boldsymbol{Q}}SO(3)$). The former kind of tangent vector fields are known as *left-invariant* and the later as *right-invariant* fields. We also observe that,

$$[\boldsymbol{K}]_{\boldsymbol{d}_i\otimes\boldsymbol{d}_j} = [\overline{\boldsymbol{K}}]_{\boldsymbol{E}_i\otimes\boldsymbol{E}_j} = \begin{bmatrix} 0 & -\overline{\kappa}_3 & \overline{\kappa}_2 \\ \overline{\kappa}_3 & 0 & -\overline{\kappa}_1 \\ -\overline{\kappa}_2 & \overline{\kappa}_1 & 0 \end{bmatrix} \tag{47}$$

Let $\boldsymbol{\kappa}$ and $\overline{\boldsymbol{\kappa}}$ represent the axial vector corresponding to the anti-symmetric matrix $\boldsymbol{K}$ and $\overline{\boldsymbol{K}}$ respectively. It can then be proved that $\overline{\boldsymbol{\kappa}} = \boldsymbol{Q}^T\boldsymbol{\kappa}$ such that if $\boldsymbol{\kappa} = \overline{\kappa}_i\boldsymbol{d}_i$, then $\overline{\boldsymbol{\kappa}} = \overline{\kappa}_i\boldsymbol{E}_i$. As in continuum mechanics, we call the quantities $\overline{\boldsymbol{K}}$ and $\overline{\boldsymbol{\kappa}}$ as *material representation*;

and $\boldsymbol{K}$ and $\boldsymbol{\kappa}$ are the *spatial representation* of the *curvature tensor* and the *curvature vector* respectively. Figs. 4 and 5 provide a physical and geometric interpretation of the discussions carried out in this section.

Similar to the curvature tensor, we summarize following relationship associated with the angular velocity vector $\boldsymbol{\omega}$ and the associated spin tensor $\boldsymbol{W}$.

$$\begin{aligned}
&\boldsymbol{W} = -\epsilon_{ijk}\overline{\omega}_k(\boldsymbol{d}_i \otimes \boldsymbol{d}_j);\\
&\overline{\boldsymbol{W}} = \boldsymbol{Q}^T\boldsymbol{W}\boldsymbol{Q} = -\epsilon_{ijk}\overline{\omega}_k(\boldsymbol{E}_i \otimes \boldsymbol{E}_j);\\
&[\boldsymbol{W}]_{\boldsymbol{d}_i\otimes\boldsymbol{d}_j} = [\overline{\boldsymbol{W}}]_{\boldsymbol{E}_i\otimes\boldsymbol{E}_j};\\
&\boldsymbol{W}\boldsymbol{Q} \in T_{\boldsymbol{Q}}SO(3) \quad \text{and} \quad \overline{\boldsymbol{W}} \in so(3); \overline{\boldsymbol{\omega}} = \boldsymbol{Q}^T\boldsymbol{\omega}.
\end{aligned} \tag{48}$$

5.2. Estimating global framed curve from limited material curvature and velocity data

We motivate the problem statement by a real life example. Consider a moving rigid body with midcurve and director triad parametrized with time. From Section 4.3, the system is governed by the following set of differential equations

$$\begin{aligned}
&\begin{bmatrix}\boldsymbol{\varphi}_{,t}\\ \boldsymbol{d}_{1,t}\\ \boldsymbol{d}_{2,t}\\ \boldsymbol{d}_{3,t}\end{bmatrix} = v(t)\begin{bmatrix}0 & \bar{t}_1 & \bar{t}_2 & \bar{t}_3\\ 0 & 0 & \overline{\kappa}_3 & -\overline{\kappa}_2\\ 0 & -\overline{\kappa}_3 & 0 & \overline{\kappa}_1\\ 0 & \overline{\kappa}_2 & -\overline{\kappa}_1 & 0\end{bmatrix}\begin{bmatrix}\boldsymbol{\varphi}\\ \boldsymbol{d}_1\\ \boldsymbol{d}_2\\ \boldsymbol{d}_3\end{bmatrix};\\
&\begin{bmatrix}\boldsymbol{\varphi}_{,t}\\ \boldsymbol{d}_{1,t}\\ \boldsymbol{d}_{2,t}\\ \boldsymbol{d}_{3,t}\end{bmatrix} = \begin{bmatrix}0 & \overline{v}_1 & \overline{v}_2 & \overline{v}_3\\ 0 & 0 & \overline{\omega}_3 & -\overline{\omega}_2\\ 0 & -\overline{\omega}_3 & 0 & \overline{\omega}_1\\ 0 & \overline{\omega}_2 & -\overline{\omega}_1 & 0\end{bmatrix}\begin{bmatrix}\boldsymbol{\varphi}\\ \boldsymbol{d}_1\\ \boldsymbol{d}_2\\ \boldsymbol{d}_3\end{bmatrix}.
\end{aligned} \tag{49}$$

In this section, we attempt to obtain estimated state space from discrete linear velocity (equivalently axial strain in case of beams) and angular velocity (or equivalently Darboux or curvature vector in case of beams). This would involve integrating Eq. (49). We assume the initial condition at $t = 0$ as $\boldsymbol{\varphi}(0) = \boldsymbol{0}$ and $\boldsymbol{d}_i(0) = \boldsymbol{d}_{i0} = \boldsymbol{E}_i$. There is no loss of generality in considering the initial condition $\boldsymbol{d}_{i0}$ as our reference frame. We assume that we have the data for linear and angular velocity expressed in $\{\boldsymbol{d}_i\}$ frame at time steps t_n such that $\overline{\boldsymbol{v}}(t_n) = \overline{\boldsymbol{v}}_n, \overline{\boldsymbol{\omega}}(t_n) = \overline{\boldsymbol{\omega}}_n$ (with $\overline{\boldsymbol{W}}_n$ being corresponding material spin matrix) and $n = 1, 2, 3, \ldots, N$. The frame $\{\boldsymbol{d}_i\}$ is to be approximated using Eq. (49). However, knowing the component of spatial quantity in current frame $\{\boldsymbol{d}_i\}$ naturally gives the associated material quantity as is clear in Eqs. (47) and (48). This is the key observation that is exploited to develop the estimation algorithm discussed in the upcoming section.

The idea is to approximate the material linear and angular velocity (recall $\mathbb{R}^3$ and $so(3)$ are linear spaces). We use these interpolated quantity to estimate our state space. From here on, the component of any material quantity will be expressed in $\{\boldsymbol{E}_i\}$ frame. Thus, for simplicity, we write $[\overline{\boldsymbol{W}}]_{\boldsymbol{E}_i\otimes\boldsymbol{E}_j} = \overline{\boldsymbol{W}}$.

5.2.1. Smooth patch estimation and gluing technique (SPEG)

In this approach, we discretized the total time span into N patches ($\overline{n} = 1, 2, \ldots, N$) or segments with center of the segment $\overline{n}$ being at t_n (except for the first and last segment). We consider the co-rotated derivatives of linear velocity and the angular velocity to vanish for each patch. Equivalently, we truncate the Taylor series expansion of the velocity fields about t_n to zeroth order, thereby reducing the system of differential Eq. (49) into a constant-coefficient system such that the solution of the differential equation gives an approximated configuration $\boldsymbol{\Phi}^h_{\overline{n}} = \left(\boldsymbol{\varphi}^h_{\overline{n}}, \boldsymbol{Q}^h_{\overline{n}}\right) \equiv \left(\boldsymbol{\varphi}^h_{\overline{n}}, \left\{\boldsymbol{d}^h_{i\overline{n}}\right\}\right) \in \mathfrak{C}$ valid in the patch $\overline{n}$. Therefore, N segments would involve solving for $12N$ constants of integration. Imposing continuity in the $(\boldsymbol{\varphi}, \{\boldsymbol{d}_i\})$ fields at the boundary between the segments gives $12(N-1)$ constraints, and an appropriate boundary condition gives the additional 12 conditions. We obtain a solution for $\overline{n}^{\text{th}}$ segment as

$$\begin{aligned}
&\boldsymbol{\varphi}^h_{\overline{n}}(t) = \boldsymbol{A}_{\overline{n}1} + \boldsymbol{A}_{\overline{n}2}t + \boldsymbol{A}_{\overline{n}3}\sin\omega_n t + \boldsymbol{A}_{\overline{n}4}\cos\omega_n t;\\
&\boldsymbol{d}^h_{i\overline{n}}(t) = \boldsymbol{B}_{\overline{n}i1} + \boldsymbol{B}_{\overline{n}i2}t + \boldsymbol{B}_{\overline{n}i3}\sin\omega_n t + \boldsymbol{B}_{\overline{n}i4}\cos\omega_n t.
\end{aligned} \tag{50}$$

In the above equation $\omega_n = \|\overline{\boldsymbol{\omega}}_n\|$. Eq. (50) yields a helix (which is smooth). This is commensurate with *Mozzi–Chasles's theorem*, the equivalent statement of which for this case would be: '*the motion of a rigid body with the co-rotational derivative of linear and angular velocity vanishing, is a screw (or helix) motion*'.

We glue the solution of each patch using heavy side function (as shown in (51)) such that the global approximated configuration $\boldsymbol{\Phi}^h = \left(\boldsymbol{\varphi}^h, \left\{\boldsymbol{d}^h_i\right\}\right) \in \mathfrak{C}$ is continuous at the point of gluing, thus justifying the name *smooth patch estimation and gluing technique* (SPEG).

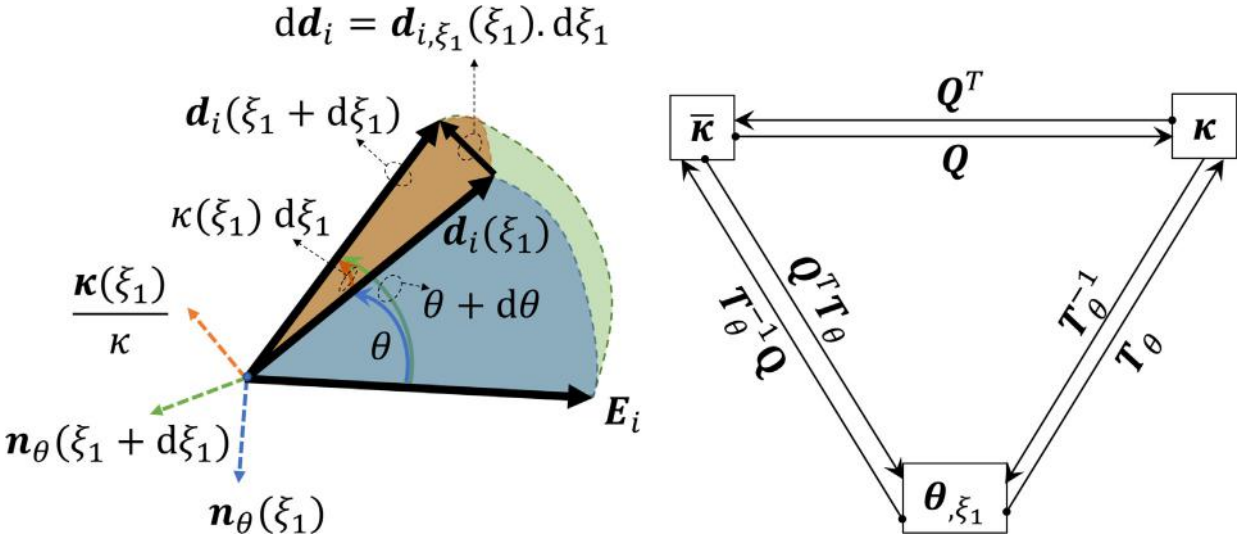

Fig. 4. Finite and infinitesimal rotations and the flowchart of various transformations.

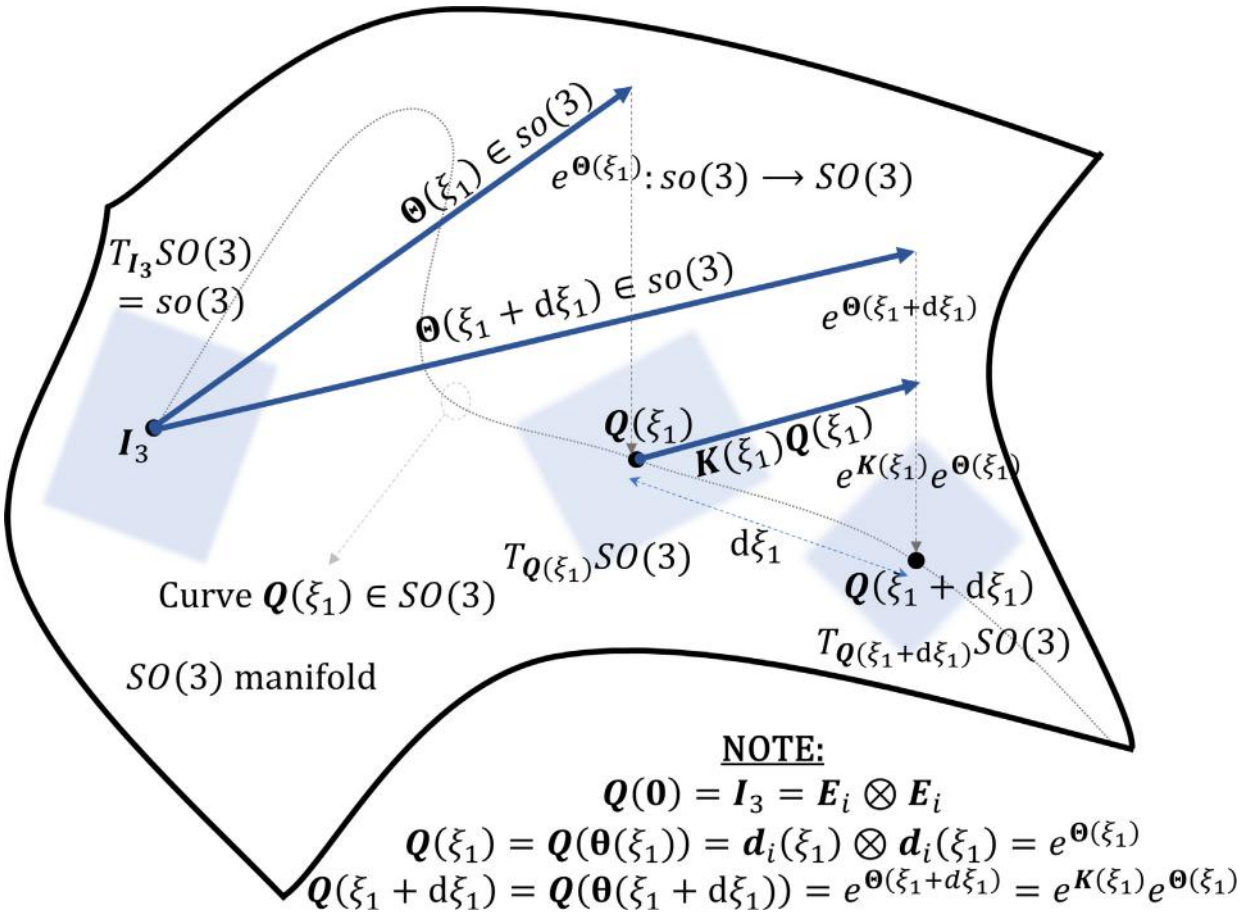

Fig. 5. Geometric representation of the finite and infinitesimal rotations, curvature tensor $\boldsymbol{K}$ and the projection from the tangent plane $T_{\boldsymbol{Q}}SO(3)$ to the manifold $SO(3)$ using exponential map.

$$\begin{aligned}\boldsymbol{\varphi}^h(t) &= \sum_{\overline{n}=1}^{N} \boldsymbol{\varphi}^h_{\overline{n}}(t)\left[H(t-\hat{t}_{\overline{n}-1}) - H(t-\hat{t}_{\overline{n}})\right];\\ \boldsymbol{d}^h_i(t) &= \sum_{\overline{n}=1}^{N} \boldsymbol{d}^h_{i\overline{n}}(t)\left[H(t-\hat{t}_{\overline{n}-1}) - H(t-\hat{t}_{\overline{n}})\right].\end{aligned} \tag{51}$$

In the equation above $H(.)$ represents Heaviside function and $\hat{t}_{\overline{n}}$ represents the right boundary of $\overline{n}^{\text{th}}$ segment (such that $\hat{t}_{\overline{n}-1} < \hat{t}_{\overline{n}}$), with $\hat{t}_0 = 0$. Appendix A.2 details the vector coefficients in Eq. (50). Interestingly, a closed form solution of the director triads can be arrived without solving the differential Eq. (49), by using our understanding of $SO(3)$ manifold as discussed in Section 5.1.2.

To carry out the discussion further, let $\boldsymbol{Q}^h(t) \in SO(3)$ represent the approximated rotation tensor with respect to $\boldsymbol{I}_3 = \boldsymbol{E}_i \otimes \boldsymbol{E}_i = \boldsymbol{d}_{0i} \otimes \boldsymbol{d}_{0i}$. For the first segment $\overline{n} = 1$, the approximated director $\boldsymbol{d}^h_{i(\overline{n}=1)} = \boldsymbol{d}^h_{i1}$ is obtained by rotating the prescribed boundary $\boldsymbol{d}_{i0} = \boldsymbol{E}_i$ by an angle $\int_0^t \omega_1 dt = \omega_1 t$ (with $\hat{t}_0 \leqslant t \leqslant \hat{t}_1$) about the unit vector $\frac{\overline{\boldsymbol{\omega}}_1}{\omega_1}$ such that,

$$\boldsymbol{d}^h_{i1}(t) = e^{\overline{\boldsymbol{W}}_1 t}\boldsymbol{d}_{i0} = \boldsymbol{Q}^h_1(t)\boldsymbol{d}_{i0} \quad \text{with} \quad \hat{t}_0 \leqslant t < \hat{t}_1. \tag{52}$$

The director triad at the right end of patch 1 becomes the boundary for the patch $\overline{n} = 2$. For patch 2 with $\hat{t}_1 \leqslant t \leqslant \hat{t}_2$ the approximate director triad $\boldsymbol{d}^h_{i2}(t)$ can be obtained by rotating $\boldsymbol{d}^h_{i1}(\hat{t}_1)$ (obtained in Eq. (52)). However, $\overline{\boldsymbol{W}}_2 \in T_{\boldsymbol{I}_3}SO(3)$ is a material tensor whose corresponding spatial counterpart associated with $T_{\boldsymbol{Q}^h_1(\hat{t}_1)}SO(3)$ is given by $\boldsymbol{W}^h_2 = \boldsymbol{Q}^h_1(\hat{t}_1)\overline{\boldsymbol{W}}_2\boldsymbol{Q}^{h^T}_1(\hat{t}_1)$ such that $\boldsymbol{W}^h_2\boldsymbol{Q}^h_1(\hat{t}_1) \in T_{\boldsymbol{Q}^h_1(\hat{t}_1)}SO(3)$. We observe that $\boldsymbol{W}^h_2\boldsymbol{Q}^h_1(\hat{t}_1)$ is a *right translated* vector field. Similarly we can obtain *left translated* vector field as $\boldsymbol{Q}^h_1(\hat{t}_1)\overline{\boldsymbol{W}}_2 \in T_{\boldsymbol{Q}^h_1(\hat{t}_1)}SO(3)$. Eqs. (53a) and (53b) gives the approximated director field for patch 2 by using *right invariant* and *left invariant* vector fields, respectively.

$$\boldsymbol{d}^h_{i2}(t) = e^{\boldsymbol{W}^h_2\cdot(t-\hat{t}_1)}\boldsymbol{d}^h_{i1}(\hat{t}_1) = e^{\boldsymbol{W}^h_2\cdot(t-\hat{t}_1)}\boldsymbol{Q}^h_1(\hat{t}_1)\boldsymbol{d}_{i0} = \boldsymbol{Q}^h_2(t)\boldsymbol{d}_{i0} \quad \text{with } \hat{t}_1 \leqslant t \leqslant \hat{t}_2; \tag{53a}$$

$$\boldsymbol{d}^h_{i2}(t) = \boldsymbol{Q}^h_1(\hat{t}_1)e^{\overline{\boldsymbol{W}}_2\cdot(t-\hat{t}_1)}\boldsymbol{d}_{i0} \text{ with } \hat{t}_1 \leqslant t \leqslant \hat{t}_2. \tag{53b}$$

Similarly for the third patch with $\boldsymbol{W}^h_3 = \boldsymbol{Q}^h_2(\hat{t}_2)\overline{\boldsymbol{W}}_3\boldsymbol{Q}^{h^T}_2(\hat{t}_2)$, we have,

$$\boldsymbol{d}^h_{i3}(t) = e^{\boldsymbol{W}^h_3\cdot(t-\hat{t}_2)}\boldsymbol{Q}^h_2(\hat{t}_2)\boldsymbol{d}_{i0} = \boldsymbol{Q}^h_3(t)\boldsymbol{d}_{i0} \quad \text{with} \quad \hat{t}_2 \leqslant t \leqslant \hat{t}_3; \tag{54a}$$

$$\boldsymbol{d}^h_{i3}(t) = \boldsymbol{Q}^h_2(\hat{t}_2)e^{\overline{\boldsymbol{W}}_3\cdot(t-\hat{t}_2)}\boldsymbol{d}_{i0} \quad \text{with} \quad \hat{t}_2 \leqslant t \leqslant \hat{t}_3. \tag{54b}$$

Along similar lines of reasoning, the solution for $\overline{n}^{\text{th}}$ patch is given by

$$\boldsymbol{d}^h_{i\overline{n}}(t) = \boldsymbol{Q}^h_{\overline{n}}(t)\boldsymbol{d}_{i0}. \tag{55}$$

where

Using *right invariant* vector field :

$$\boldsymbol{Q}^h_{\overline{n}}(t) = e^{\boldsymbol{W}^h_{\overline{n}}\cdot(t-\hat{t}_{\overline{n}-1})}\boldsymbol{Q}^h_{\overline{n}-1}(\hat{t}_{\overline{n}-1}) \quad \text{with} \quad \hat{t}_{\overline{n}-1} \leqslant t \leqslant \hat{t}_{\overline{n}}; \tag{56a}$$

Using *left invariant* vector field :

$$\boldsymbol{Q}^h_{\overline{n}}(t) = \boldsymbol{Q}^h_{\overline{n}-1}(\hat{t}_{\overline{n}-1})e^{\overline{\boldsymbol{W}}_n\cdot(t-\hat{t}_{\overline{n}-1})} \quad \text{with} \quad \hat{t}_{\overline{n}-1} \leqslant t \leqslant \hat{t}_{\overline{n}}. \tag{56b}$$

The spatial curvature tensor $\boldsymbol{W}_n^h$ in Eq. (56a) is given below. Note that $\boldsymbol{W}_n^h$ is not a function of time for a given patch $\overline{n}$ and unlike the material tensor $\overline{\boldsymbol{W}}_n$, the spatial curvature tensor is an approximated quantity.

$$\boldsymbol{W}_n^h = \boldsymbol{Q}_{\overline{n}-1}^h(\hat{t}_{\overline{n}-1})\overline{\boldsymbol{W}}_n\boldsymbol{Q}_{\overline{n}-1}^{h^T}(\hat{t}_{\overline{n}-1}). \tag{57}$$

The global approximated rotation tensor is then given by,

$$\boldsymbol{Q}^h(t) = \sum_{\overline{n}=1}^{N}\boldsymbol{Q}_{\overline{n}}^h(t)\left[H(t-\hat{t}_{\overline{n}-1}) - H(t-\hat{t}_{\overline{n}})\right]. \tag{58}$$

From Eqs. (49) and (56b), the approximated position vector for patch $\overline{n}$ is obtained as,

$$\boldsymbol{\varphi}_{\overline{n}}^h(t) = \left[\int_{\hat{t}_{\overline{n}-1}}^{t} e^{\overline{\boldsymbol{W}}_n t}\mathrm{d}t\right].\overline{\boldsymbol{v}}_n + \sum_{k=1}^{\overline{n}-1}\left[\int_{\hat{t}_{k-1}}^{\hat{t}_k} e^{\overline{\boldsymbol{W}}_k t}\mathrm{d}t\right].\overline{\boldsymbol{v}}_k. \tag{59}$$

Fig. 6 gives geometric interpretation of the discussion so far.

Remarks: This approach has following noteworthy geometric interpretations:

Remark 5.2.1.1. Consider the $\overline{n}^{\text{th}}$ patch where the approximated configuration $\boldsymbol{\Phi}_{\overline{n}}^h$ is parametrized by $t \in [t_{\overline{n}-1}, t_{\overline{n}}]$. The co-rotated derivative of angular velocity being zero implies that the angular velocity is parallel-transported along a curve $\boldsymbol{Q}_{\overline{n}}^h(t)$ on the manifold $SO(3)$ such that the approximated angular velocity $\boldsymbol{\omega}_{\overline{n}}^h$ at time t is given as,

$$\boldsymbol{\omega}_{\overline{n}}^h(t) = \boldsymbol{Q}_{\overline{n}}^h(t)\overline{\boldsymbol{\omega}}_n = \boldsymbol{Q}_{\overline{n}}^h(t)\boldsymbol{Q}_{\overline{n}}^{h^T}(\hat{t}_n)\boldsymbol{\omega}_n^h. \tag{60}$$

The vector $\boldsymbol{\omega}_n^h$ is the associated axial vector for the spatial tensor $\boldsymbol{W}_n^h$. From the equation above and Eq. (57), we observe that the spatial angular velocity $\boldsymbol{\omega}_n^h = \boldsymbol{Q}_{\overline{n}}^h(t_n)\overline{\boldsymbol{\omega}}_n$ and the associated spin tensor $\boldsymbol{W}_n^h$ are approximate quantities. It is interesting to observe that $\|\boldsymbol{\omega}_n^h\| = \|\overline{\boldsymbol{\omega}}_n\| = \omega_n$.

Remark 5.2.1.2. The solution obtained above is free of singularity (unlike Frenet frame). If the angular velocity measurement for the $\overline{n}^{\text{th}}$ patch is zero (implying point of inflection), we have the solution of the form,

$$\lim_{\boldsymbol{\omega}_n \to \boldsymbol{0}} \boldsymbol{\varphi}_{\overline{n}}^h(t) = \left(C_{\overline{n}i4} + t\left(C_{\overline{n}ij}\overline{v}_{nj}\right)\right)\boldsymbol{E}_i; \tag{61a}$$

$$\lim_{\boldsymbol{\omega}_n \to \boldsymbol{0}} \boldsymbol{d}_{\overline{n}}^h(t) = C_{\overline{n}ji}\boldsymbol{E}_j = \boldsymbol{d}_{i(\overline{n}-1)}^h(\hat{t}_{\overline{n}-1}). \tag{61b}$$

Solution of the form above suggests a local linear solution for the approximated position vector and a constant solution for the approximated director triads. However, if $\overline{\boldsymbol{v}}_n = \boldsymbol{0}$ and $\overline{\boldsymbol{\omega}}_n = \boldsymbol{0}$, the approximated local solution is a point (the object is stationary) with a fixed director triad given by Eq. (61b) and the position vector reduces to,

$$\lim_{\substack{\boldsymbol{v}_n \to \boldsymbol{0} \\ \boldsymbol{\omega}_n \to \boldsymbol{0}}} \boldsymbol{\varphi}_{\overline{n}}^h(t) = C_{\overline{n}i4}\boldsymbol{E}_i = \boldsymbol{\varphi}_{\overline{n}-1}^h(\hat{t}_{\overline{n}-1}). \tag{62}$$

Similarly, the limiting case of solution with $\overline{\boldsymbol{v}}_n = \boldsymbol{0}$ represents a rotating rigid body with no translation. In case where $\overline{\boldsymbol{v}}_n \neq \boldsymbol{0}$ and $\overline{\boldsymbol{\omega}}_n \neq \boldsymbol{0}$, the solution represented by Eq. (50) is a helix. Thus, if the moving object follows a helix exactly with constant speed, we need only one data point along with the prescribed boundary condition to give exact state space (provided there is no noise in the data). Lastly, the accuracy of global solution depends on the nature of data. If the data is representative of the local configuration of a patch, a good approximation is obtained.

5.2.2. Other higher order approximation techniques

In the SPEG technique discussed above, the approximated linear and angular velocity fields were C^{-1} continuous. The advantage of the SPEG technique lies in the existence of a closed-form solution, making it a desirable approach provided the linear and angular velocity data (or equivalently, strain and curvature data in case of shape sensing of rods) does not vary too much along the patch. Todd et al. [20] and Chadha and Todd [21,24] used SPEG to develop shape reconstruction of rods and observed that

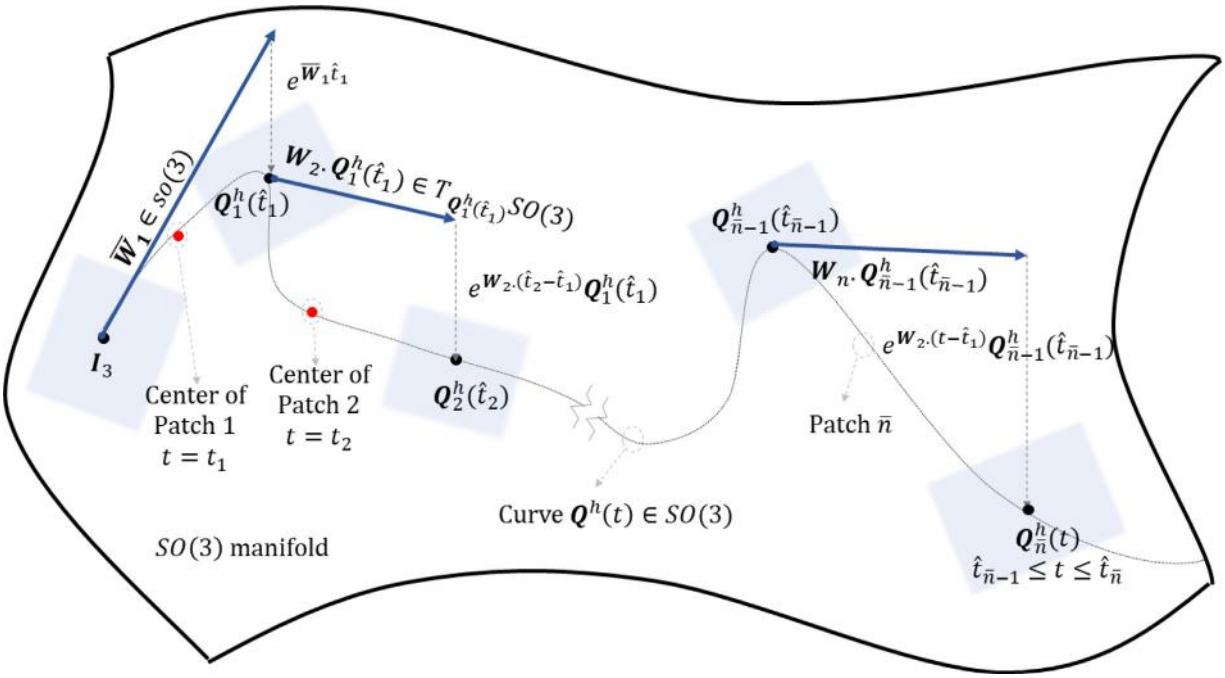

Fig. 6. Geometric representation of SPEG.

a fairly accurate solution is obtained in such case. However, if the system is more dynamic (like a UAV), a higher order approximation of linear and angular velocity field is desirable. We can approximate these fields using Lagrangian Polynomial, cubic splines, Hermite polynomial interpolation, and moving least square (MLS), to name a few.

Note that the data for linear and angular velocity are obtained in $\{\boldsymbol{d}_i\}$ frame, which is time dependent. However, to numerically integrate Eq. (49), we utilize the approximated fields of the components $\overline{v}_i^h$ and $\overline{\omega}_i^h$ (we do not approximate the spatial linear velocity and the angular velocity vectors). Equivalently, we are interpolating the material linear velocity $\overline{\boldsymbol{v}}(t) = \overline{v}_i \boldsymbol{E}_i$ and the material angular velocity $\overline{\boldsymbol{\omega}}(t) = \overline{\omega}_i \boldsymbol{E}_i$. Let $\overline{\boldsymbol{v}}^h(t)$ and $\overline{\boldsymbol{\omega}}^h(t)$ (with $\overline{\boldsymbol{W}}^h(t)$ being the corresponding spin tensor) represent the approximated material linear and angular velocity. The estimated configuration is obtained as

$$\begin{aligned} \boldsymbol{Q}^h(t) &= e^{\int_0^t \overline{\boldsymbol{W}}^h(t)\mathrm{d}t}; \\ \boldsymbol{\varphi}^h(t) &= \int_0^t \boldsymbol{Q}^h(t).\overline{\boldsymbol{v}}^h(t)\mathrm{d}t, \end{aligned} \tag{63}$$

with,

$$\int_0^t \overline{\boldsymbol{W}}^h(t)\mathrm{d}t \in so(3). \tag{64}$$

5.2.3. Error quantification

We quantify the error $e_{\boldsymbol{\varphi}}(t)$ in the position vector by the usual Euclidean norm of difference in the exact and estimated position vector,

$$e_{\boldsymbol{\varphi}}(t) = \|\boldsymbol{\varphi}(t) - \boldsymbol{\varphi}^h(t)\|; \tag{65a}$$

$$\mathrm{RMS}_{\boldsymbol{\varphi}} = \sqrt{\frac{\sum_{k=1}^{M} e_{\boldsymbol{\varphi}}^2(t_k)}{M}}. \tag{65b}$$

Similarly, we define error in each director as,

$$e_{\boldsymbol{d}_i}(t) = \|\boldsymbol{d}_i(t) - \boldsymbol{d}_i^h(t)\|; \tag{66a}$$

$$\mathrm{RMS}_{\boldsymbol{d}_i} = \sqrt{\frac{\sum_{k=1}^{M} e_{\boldsymbol{d}_i}^2(t_k)}{M}}. \tag{66b}$$

Local homeomorphism (refer to Section 3.2.2) of exponential map allows us to define *Reimannian metric* on $SO(3)$ that evaluates the deviation between the approximated rotation tensor $\boldsymbol{Q}^h(t)$ and the exact rotation tensor $\boldsymbol{Q}(t)$ by measuring the length of geodesic between them. The error is associated with the amount of rotation $\boldsymbol{Q}_{\mathrm{error}}(t)$ required to align $\boldsymbol{Q}^h(t)$ with $\boldsymbol{Q}(t)$ such that,

$$\boldsymbol{Q}(t) = \boldsymbol{Q}_{\mathrm{error}}(t)\boldsymbol{Q}^h(t). \tag{67}$$

Let $\boldsymbol{Q}_{\mathrm{error}}(t)$ be parametrized by $\boldsymbol{\theta}_e = \theta_e \boldsymbol{n}_{\theta_e}$ such that $\theta_e \in [0, \pi)$. We define the error $e_{\boldsymbol{Q}}$ as,

$$e_{\boldsymbol{Q}}(t) = \left\langle \boldsymbol{Q}, \boldsymbol{Q}^h \right\rangle = \theta_e(t) = \|\log(\boldsymbol{Q}_{\mathrm{error}}(t))\| \in [0, \pi); \tag{68a}$$

$$\mathrm{RMS}_{\boldsymbol{Q}} = \sqrt{\frac{\sum_{k=1}^{M} e_{\boldsymbol{Q}}(t_k)^2}{M}}. \tag{68b}$$

In the equation above, $\langle .,. \rangle : SO(3) \times SO(3) \to [0, \pi)$ defines a bi-invariant (refer to Eqs. (70e) and (70f) below) Reimannian metric such that for any $\boldsymbol{Q}_1, \boldsymbol{Q}_2 \in SO(3)$,

$$\langle \boldsymbol{Q}_1, \boldsymbol{Q}_2 \rangle = \|\log\left(\boldsymbol{Q}_1 \boldsymbol{Q}_2^T\right)\|. \tag{69}$$

For any $\boldsymbol{Q}_1, \boldsymbol{Q}_2, \boldsymbol{Q}_3 \in SO(3)$ the metric defined above has following properties:

$$\text{Non-negativity}: \ \langle \boldsymbol{Q}_1, \boldsymbol{Q}_2 \rangle \in [0, \pi) \tag{70a}$$

$$\text{Identity of indiscernibles}: \ \langle \boldsymbol{Q}_1, \boldsymbol{Q}_2 \rangle = 0 \iff \boldsymbol{Q}_1 = \boldsymbol{Q}_2 \tag{70b}$$

$$\text{Symmetry}: \ \langle \boldsymbol{Q}_1, \boldsymbol{Q}_2 \rangle = \langle \boldsymbol{Q}_2, \boldsymbol{Q}_1 \rangle \tag{70c}$$

$$\text{Triangle inequality}: \ \langle \boldsymbol{Q}_1, \boldsymbol{Q}_2 \rangle \leqslant \langle \boldsymbol{Q}_1, \boldsymbol{Q}_3 \rangle + \langle \boldsymbol{Q}_3, \boldsymbol{Q}_2 \rangle \tag{70d}$$

$$\text{Right invariant}: \ \langle \boldsymbol{Q}_1 \boldsymbol{Q}_3, \boldsymbol{Q}_2 \boldsymbol{Q}_3 \rangle = \langle \boldsymbol{Q}_1, \boldsymbol{Q}_2 \rangle \tag{70e}$$

$$\text{Left invariant}: \ \langle \boldsymbol{Q}_3 \boldsymbol{Q}_1, \boldsymbol{Q}_3 \boldsymbol{Q}_2 \rangle = \langle \boldsymbol{Q}_1, \boldsymbol{Q}_2 \rangle \tag{70f}$$

Refer to Park [32] for more details on this metric. The paper by Huynh [33] serves as a great reference to understand various kinds of metric on $SO(3)$. Huynh [33] also provides proof for the properties stated above.

5.3. Similarities in the path estimation of rigid body (or swarm of rigid bodies) and shape reconstruction of slender structure (like rods)

A rigid body motion and a beam with rigid Euler-Bernoulli's cross-section is defined by an identical configuration space $\mathfrak{C} := \mathbb{R}^3 \times SO(3)$. The Cosserat beam is defined by a midcurve curve $\boldsymbol{\varphi}$ and the director triad field $\{\boldsymbol{d}_i\}$ that defines the orientation of the cross-section. However, the configuration of the beam $\boldsymbol{\Phi}_1 \in \mathfrak{C}$ is parametrized by the undeformed arc length of the midcurve, lets call it $s \in \mathbb{R}^+$, and the configuration of the moving rigid body $\boldsymbol{\Phi}_2 \in \mathfrak{C}$ is parametrized by time $t \in \mathbb{R}^+$, such that

$$\begin{aligned} \boldsymbol{\Phi}_1(s) &:= \left\{(\boldsymbol{\varphi}(s), \boldsymbol{Q}(s))| \quad \boldsymbol{\varphi} : \mathbb{R}^+ \to \mathbb{R}^3, \quad \boldsymbol{Q} : \mathbb{R}^+ \to SO(3)\right\} \in \mathfrak{C}; \\ \boldsymbol{\Phi}_2(t) &:= \left\{(\boldsymbol{\varphi}(t), \boldsymbol{Q}(t))| \quad \boldsymbol{\varphi} : \mathbb{R}^+ \to \mathbb{R}^3, \quad \boldsymbol{Q} : \mathbb{R}^+ \to SO(3)\right\} \in \mathfrak{C}. \end{aligned} \tag{71}$$

If ξ_1 represents the arclength in the deformed state of the beam or the distance traveled by the moving object, then an analogy can be observed between the axial strain of the midcurve $e(s)$ for the beam and the velocity $v(t)$ of the moving object, such that, $\xi_{1,s} = 1 + e(s)$ for beams, and $\xi_{1,t} = v(t)$ in case of a moving rigid body.

Like the configuration space, the tangent space of the two systems is identical. The equivalent of angular velocity (spin) tensor $\boldsymbol{W}(t) = \boldsymbol{Q}_{,t}\boldsymbol{Q}^T$ is the spin tensor corresponding to the Darboux vector (also called the curvature tensor) $\boldsymbol{K}(s) = \boldsymbol{Q}_{,s}\boldsymbol{Q}^T$. Therefore, the problem of shape reconstruction of beam from finite number of surface strain gauge readings bears a striking similarity with the path estimation of rigid body motion using discrete linear and angular velocity data. In case of path estimation, the data is obtained in the form of Euler angles (or quaternions) and their derivatives (from the IMU and other sensors), whereas in case of shape sensing, the strain gauge data can be used to obtain the sectional curvatures and midcurve strains. Furthermore, the problem of *dead reckoning* is common in case of path estimation and shape sensing (refer to [21]). Chadha and Todd [21] presents the method to obtain cross-sectional curvatures and finite strains using strain gauges attached to the surface and a more recent work of Chadha and Todd [34], explores the relationship between scalar strain gauge readings with the finite strain parameters.

A geometrically-exact *Kirchhoff* beam and a rigid body can be defined by an *adapted* frame. If the torsion angle is zero along the beam or if the roll angle field vanishes (which is seldom in case of rigid body motion), SMAF is sufficient to define the orientation. Presence of torsion field in the beam and roll angle in the rigid body demands GMAF to define the orientation.

A more interesting case arises when we consider swarm of rigid-bodies (say drones). If the swarm is a *rigid-formation*, the relative positions of *follower* drone is fixed (with vanishing co-rotational derivative) and pre-defined with respect to the *leader* drone. If the *rigid-formation* is planar, the orientation of the plane and the position vector of the leader drone defines the configuration of the system. This is analogous to *Simo-Reissner* beam (refer

to: Simo [18] and Reissner [19]) that has *rigid cross-section* and is allowed to have shear deformation (unlike Euler-Bernoulli beam, where the cross-section is perpendicular to the midcurve and shear deformations are ignored). In a *leader-follower* model of drone formations, the *follower* drones need not have a fixed relative position with respect to the *leader* drone. However, if the relative positions of follower drones are pre-defined (that is useful for drone light-shows that have gained recent popularity), the system maintains its single-manifold character. This system is similar to *Simo-Reissner* beam with in-plane and out-of-plane cross-sectional deformation with warping and Poisson's transformation being pre-defined. Material frame (MF) can be used to define orientation in these type of problems. The paper by Chadha and Todd [34] is dedicated to developing a generalized single-manifold beam kinematics that includes *fully coupled Poisson's and warping effect* (such that the cross-sectional deformation is pre-defined to maintain single-manifold nature of problem).

The compact approach in defining the shape of swarm at any given time is accomplished using partial differential equation. For a system like swarm of drones, trajectory tracking is essential to define controls for the system so that the shape of swarm converges to the solution of prescribed differential equation at a given time. Defining the shape as a solution to governing differential equation is compact, communication and memory efficient, and it helps in developing a local corrective algorithm (distributed control) where one drone corrects its position based on the position of neighboring drones. This process is very much similar to obtaining warping function from the Neumann boundary value problem corresponding to warping in beam. The local corrective algorithm in case of swarm of drones is comparable to the compatibility conditions in solid mechanics.

Table 1
Various approach to interpolate the material linear and angular velocity data.

Cases	Interpolation method
Case 1	C^{-1} approximation (constant over the patch $\overline{n}$ of SPEG)
Case 2	Cubic Hermite
Case 3	C^0 approximation
Case 4	Moving least square approximation (MLS)
Case 5	Cubic B-Spline
Case 6	Quadratic B-Spline

5.4. Illustration and simulation

We simulate the path of a moving rigid body like UAV. We consider the pitch, yaw and roll angle fields parametrized by $t \in [0, \bar{t}]$ calibrated with respect to $\{\boldsymbol{E}_i\}$ frame,

$$\begin{aligned}
&\phi_p(t) = 0.5\sin(0.7\bar{t}) + \tfrac{\pi}{2}\left[\cos\left(\tfrac{\pi t}{\bar{t}}\right) + \sin\left(\tfrac{\pi t}{\bar{t}}\right).\left(1 - \sin\left(\tfrac{3.5\pi t}{\bar{t}}\right)\right)\right];\\
&\phi_y(t) = 4 + \tfrac{1}{25}(t - \bar{t}) + \sin(t) + \pi\sin\left(\tfrac{4\pi t}{\bar{t}}\right);\\
&\phi_r(t) = 0.1\left(\pi\sin\left(\tfrac{4\pi t}{\bar{t}}\right) + \sin(t)\right);\\
&\overline{v}_1(t) = 1 + 0.15\sin(0.3t) + 0.2\cos\left(\tfrac{4\pi t}{2\bar{t}}\right);\\
&\overline{v}_2(t) = \overline{v}_3 = 0.
\end{aligned} \tag{72}$$

The rigid-body motion defined by (72) is similar to Kirchhoff beam kinematics. A GMAF is sufficient to frame this path because $\overline{v}_2(t) = \overline{v}_3(t) = 0$. Thus, we obtain the angular velocity components $\overline{\omega}_i$ from the assumed Euler angles in Eq. (72) using the results obtained in Section 4.1.2 (except that the independent parameter here is time t). We can equivalently consider unit quaternion field and obtained the angular velocity using Eqs. 86a, 86b and 86c. The exact rotation tensor is obtained by using Eq. (26). Note that for this example $\{\boldsymbol{d}_1, \boldsymbol{d}_2, \boldsymbol{d}_3\} \equiv \{\boldsymbol{T}, \boldsymbol{Y}_g, \boldsymbol{P}_g\}$. At $t = 0$, the initial conditions are $\boldsymbol{d}_i(0) = \boldsymbol{d}_{i0} = \boldsymbol{E}_i$. The exact position vector is then obtained as,

$$\boldsymbol{\varphi}(t) = \int_0^t \overline{v}_1(k)\boldsymbol{d}_1(k)\mathrm{d}k. \tag{73}$$

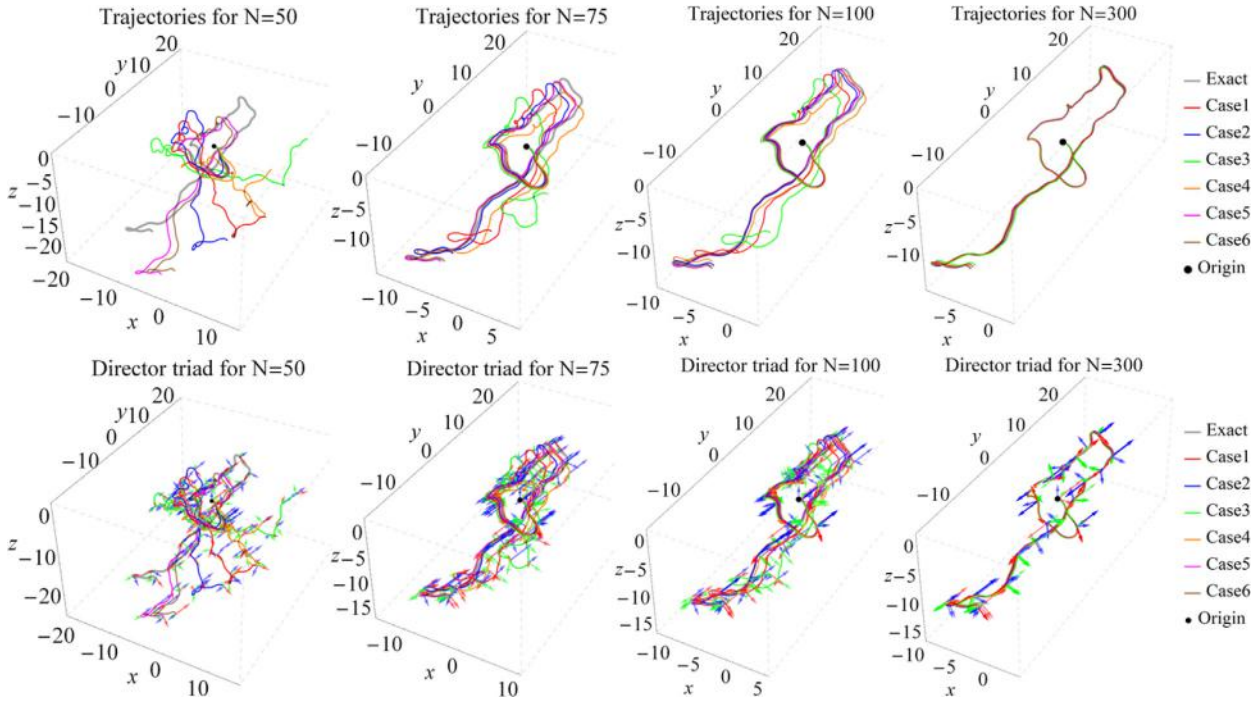

Fig. 7. Estimated trajectory and orientation of the rigid body (or equivalently the cross-section of slender rod).

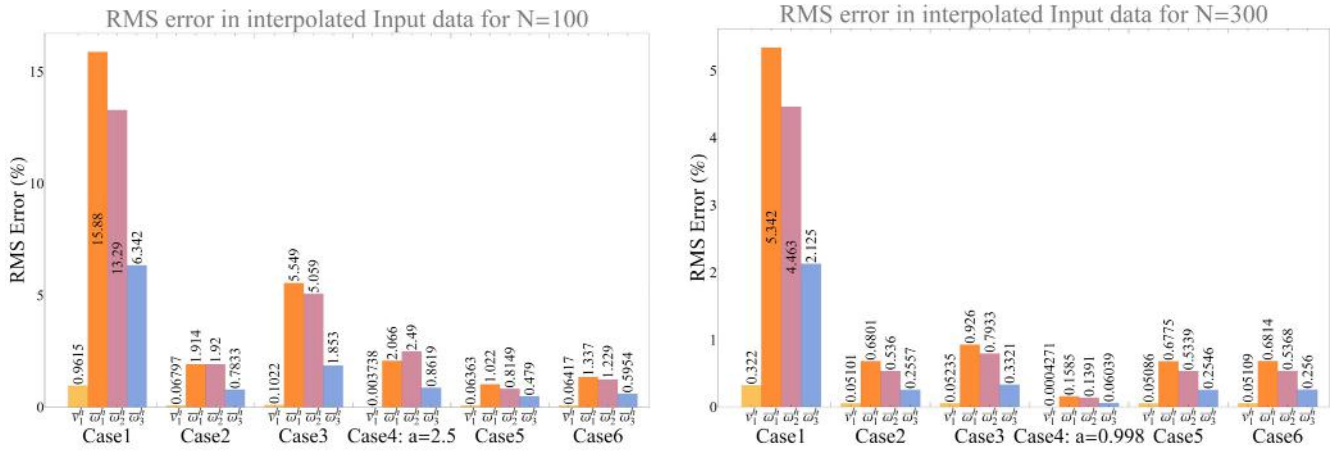

(a) $N=100$ (b) $N=300$

Fig. 8. RMS error in the approximated material linear and angular velocity fields by various approaches.

We consider $t_0 = 100$ s and number of discrete data points as N with t_n representing the time corresponding to n^{th} data point. We assume $t_1 = 0.25$ s and $t_N = (\bar{t} - 0.25)$ s. The time steps in between t_1 and t_n are uniformly spaced. We use 6 different interpolation techniques listed in Table 1 to approximate the material linear and angular velocity.

Consider the following points:

1. In case 1, the data $\overline{\boldsymbol{v}}_n$ and $\overline{\boldsymbol{\omega}}_n$ are assumed constant over the patch $\overline{n}$ as described in Section 5.2.1. The estimated configuration space using SPEG is the same as the configuration space obtained using Eq. (63) with $\overline{\boldsymbol{v}}_n^h$ and $\overline{\boldsymbol{\omega}}_n^h$ being C^{-1} approximation of the data over the patch $\overline{n}$. This technique was used by Chadha and Todd [21] to develop shape sensing algorithm for beams.
2. Readers can refer to chapter 3 of Bartels et al. [35] for more information on Cubic Hermite and B-Spline interpolation. Case 3 represents the data being linearly interpolated between two time steps t_n and t_{n+1}.
3. We briefly describe the MLS approach here. Let $\boldsymbol{P}(t) = \{1, t, t^2, \ldots, t^m\}^T$ represent set of m^{th} order polynomial set and $W(t - t_n)$ represent the moving weight function, then the approximate linear velocity component $\overline{v}_i^h(t)$ is given as,

$$\begin{aligned} \overline{v}_i^h(t) &= \boldsymbol{P}^T(t_n)\boldsymbol{M}^{-1}\sum_{n=1}^{N}\boldsymbol{P}(t_n)\overline{v}_{ni}W(t-t_n); \\ M &:= \text{Moment matrix} = \sum_{n=1}^{N}\boldsymbol{P}(t_n)\boldsymbol{P}^T(t_n)W(t-t_n). \end{aligned} \tag{74}$$

We have used cubic B-spline weight function, such that

$$W(t-t_n) = W(z_n) = \begin{cases} \frac{2}{3} - 4z_n^2 + 4z_n^3, & \text{for } 0 \leqslant z_n \leqslant 0.5 \\ \frac{4}{3} - 4z_n + 4z_n^2 - \frac{4}{3}4z_n^3, & \text{for } 0.5 \leqslant z_n \leqslant 1; \\ 0 & \text{otherwise} \end{cases} \tag{75}$$

$z_n = \frac{|t-t_n|}{a}$.

The term a in the equation above is the support size. For m^{th} order basis set, the weight function must be spread enough to cover at least $(m+1)$ data points. This fact is used to evaluate the support size. The accuracy of MLS approach depends on the choice of support size and the order of polynomial. In a similar fashion, the approximate angular velocity fields $\overline{\omega}_i^h(t)$ is obtained. Interested readers can refer to the landmark paper on interpolation of surface using MLS approach by Lancaster and Salkauskas [36]. A paper by Levin [37] discusses how MLS is the near-best approach towards interpolation. MLS approximation became popular in the field of applied mechanics after

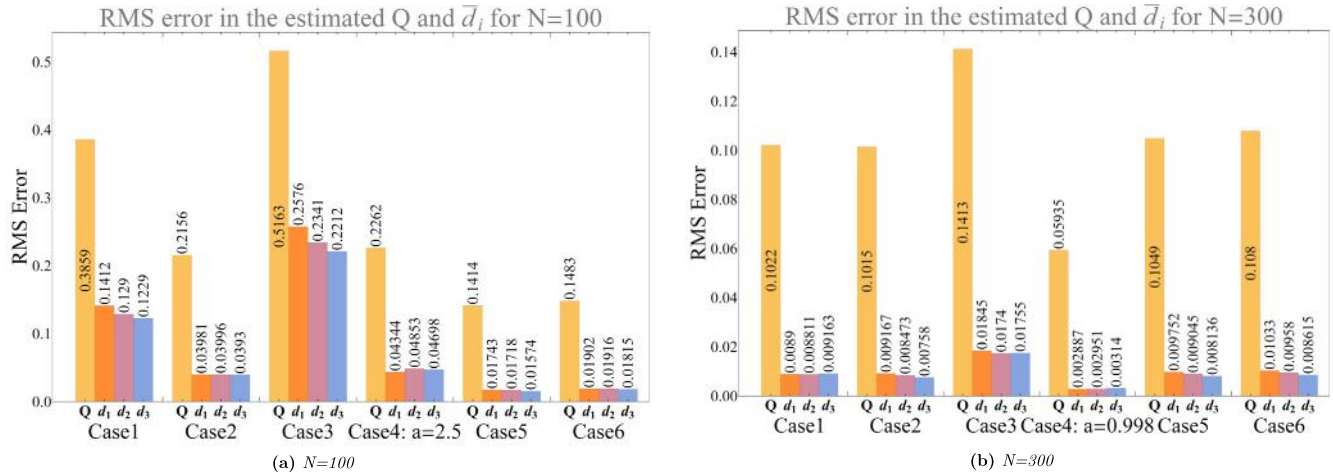

(a) $N=100$ (b) $N=300$

Fig. 9. RMS error in the estimated $\boldsymbol{Q}$ and $\boldsymbol{d}_i$ by various approaches.

it was used to develop Meshfree finite element analysis (refer Belytschko et al. [38] and Chen et al. [39]).

We consider N = 20, 50, 75, 100, 300 and 500 to compare various approaches. The idea is to estimate the configuration space $\left(\boldsymbol{\varphi}^h(t), \mathbf{Q}^h(t)\right)$ using Eq. (63) (for all cases except Case 1) and (51) (for Case 1). The spatial linear and angular velocity is estimated by left translating approximated material linear and angular velocity as,

$$\begin{aligned} \boldsymbol{v}^h(t) &= \mathbf{Q}^h \overline{\boldsymbol{v}}^h(t); \\ \boldsymbol{\omega}^h(t) &= \mathbf{Q}^h \overline{\boldsymbol{\omega}}^h(t). \end{aligned} \tag{76}$$

Fig. 7 demonstrates the estimated configuration (the trajectory and the orientation of object at 20 uniformly spaces time steps) for N = 50, 75, 100 and 300 obtained using interpolation methods mentioned in Table 1. The estimated shape converges with the increase of data points as expected. Fig. 8 shows RMS errors in the approximated material linear and angular velocity $(\overline{\boldsymbol{v}}^h, \overline{\boldsymbol{\omega}}^h)$ and the estimated position vector, director triads and rotation tensor for N = 100 and 300, calculated using M = 500 in Eqs. (65b), (66b) and (68b). Excellent estimates are obtained for N = 100 with the error: $\text{RMS}_{\mathbf{Q}} = \{0.386, 0.216, 0.516, 0.226, 0.141, 0.148\}$ radian and $\text{RMS}_{\boldsymbol{\varphi}} = \{2.237, 0.570, 4.193, 0.669, 0.309, 0.326\}$ m for case 1 to 6 respectively. The RMS error further reduces with increase of data points, as observed in Fig. 9. Fig. 9 and 10 show the error fields $e_{\boldsymbol{\varphi}}(t), e_{\mathbf{Q}}(t)$ and $e_{\boldsymbol{d}_i}(t)$ obtained using the error definition in Eqs. (65a), (66a) and (68a). Fig. 11 shows comparison of RMS error in the configuration space for different interpolation approaches with increasing number of sensors (see Fig. 12).

Here are the important observations:

1. As is clear from Fig. 13, the algorithm is convergent.
2. The MLS (case 4) and Cubic spline interpolation (case 5 and 6) are amongst the best approaches to estimate the state space. This is because Case 4 and 5 (and 6) interpolated the input data better than other approaches.

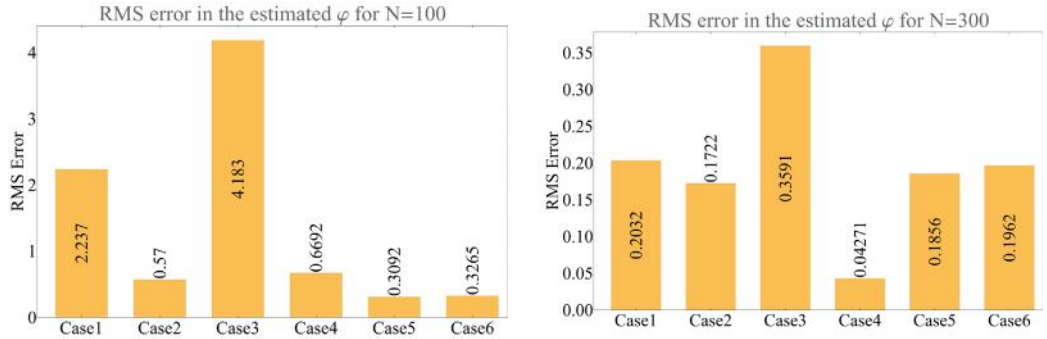

(a) *N=100* (b) *N=300*

Fig. 10. RMS error in the estimated $\boldsymbol{\varphi}$ by various approaches.

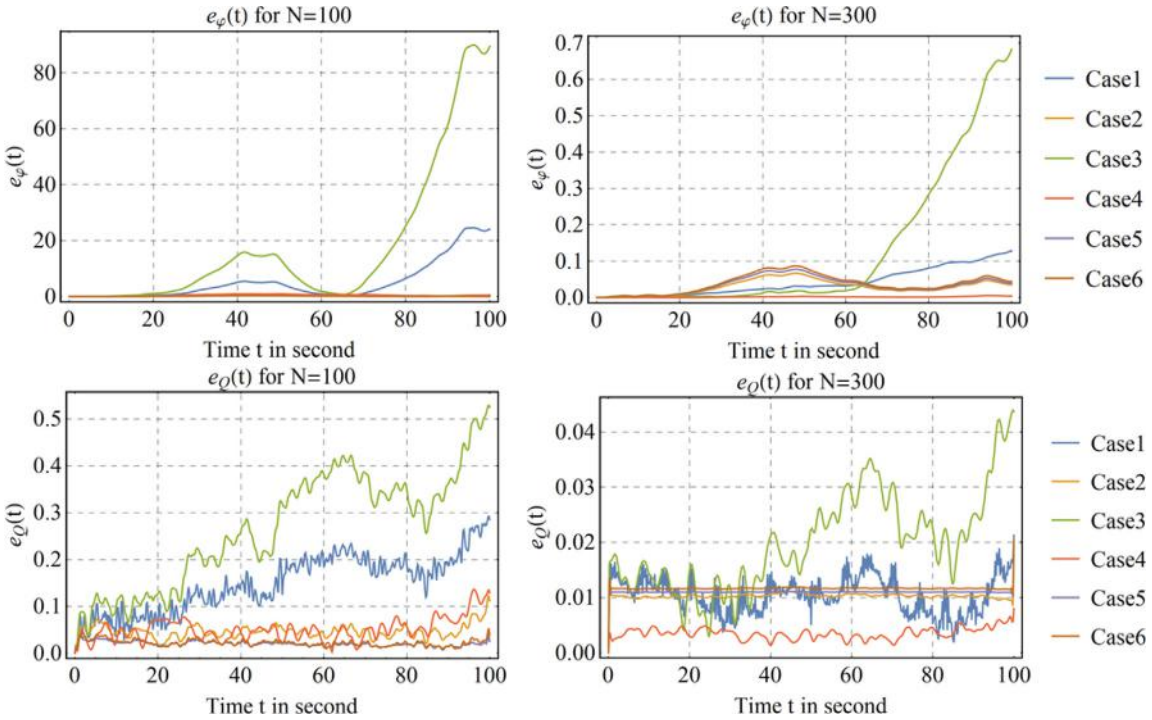

Fig. 11. Error e_{φ} and $e_{\mathbf{Q}}$ for $N = 100$ and $N = 300$.

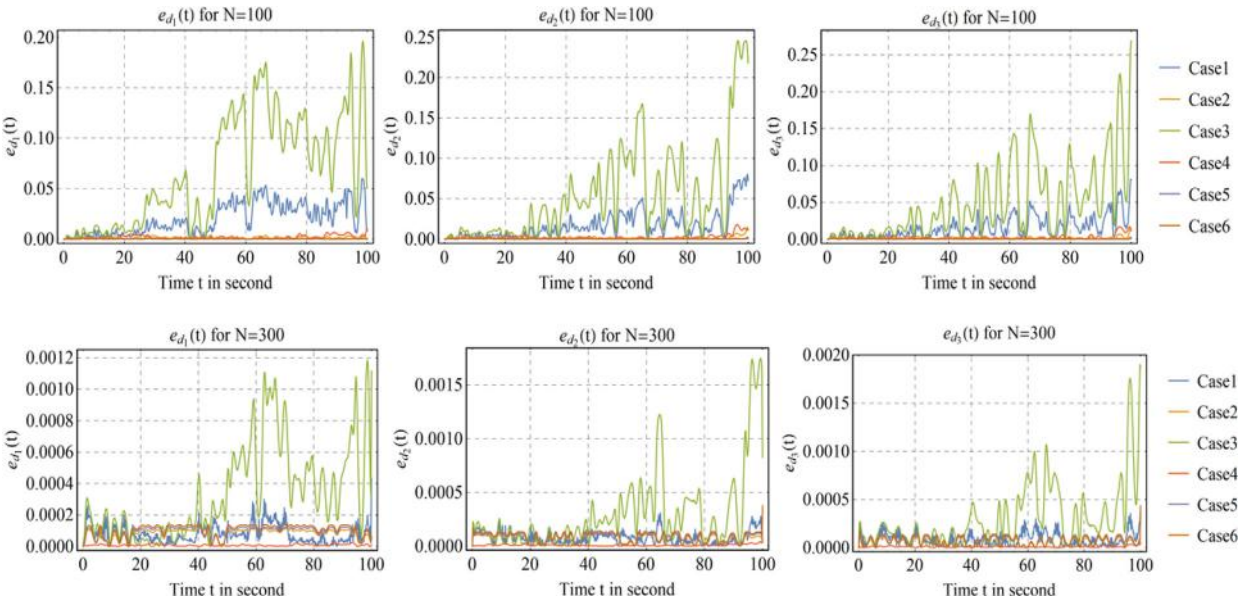

Fig. 12. Error e_{d_i} for $N = 100$ and $N = 300$.

3. Proper choice of support size and polynomial order in MLS method can drastically reduce the error. In this case, we have used polynomial of 2nd order with support size of a = 15.7, 5.08, 3.09, 2.5 and 0.998; for N = 20, 50, 75, 100 and 300 respectively.
4. Linear interpolation of input data (case 3) is the worst performer in terms of the configuration space estimate.
5. Despite having highest RMS error in estimating the input data, SPEG technique (case 1) performs fairly well (better than case 3 that gives highest error) at the estimation of configuration. The advantage of SPEG is existence of a closed form solution as discussed in Section 5.2.1 whereas other higher order approaches (case 2–5) includes numerical integration (Eq. (63)) to obtain the configuration space. We also observe that the error propagates along the trajectory of object attaining maximum value at the farthest end from the point of initial condition.
6. Cubic and quadratic B-splines gives nearly same result. With increase in number of data, B-spline approximation and Cubic Hermite approximations converges.
7. The error discussed here is purely due to the numerical algorithm used to estimate the configuration space. However, in real time, the noise in the measurement must be considered. Another source of error might be in the uncertainty of initial condition (especially in shape sensing of beams: refer to Chadha and Todd [21]).

6. Applications in computer graphics

Theory of curves and moving frames has found a dominant place in generating computer graphics, including but not limited to ribbons, orientation of camera frames and quantum waveguide construction, CAD-CAM modeling and animations (refer [11,13,35]). Extruding a cross-section along a straight center line has long been used in CAD modeling. In this section, we present few applications of various types of framed space curves discussed so far in computer graphics.

6.1. Double helix intertwining a space curve

We elucidate the construction of double helix using GMAF. Consider the pitch $\phi_p(\xi_1)$ and yaw angle $\phi_y(\xi_1)$ field corresponding to the space curve $\boldsymbol{\varphi}(\xi_1)$ with total length l_0, parametrized by the arclength $\xi_1 \in [0, l_0]$ such that,

$$\boldsymbol{\varphi}(\xi_1) = \int_0^{\xi_1} \boldsymbol{T}(k)\mathrm{d}k. \tag{77}$$

In the above equation, $\boldsymbol{T}(\xi_1)$ represents the tangent vector field of the curve, the component of which can be obtained from either Eq. (25) or (26) (note than $\boldsymbol{T}(\xi_1)$ is sufficient to define the mid-curve). Let r and c represents the radius and total number of windings (that can be fractional) of double helix respectively. We can

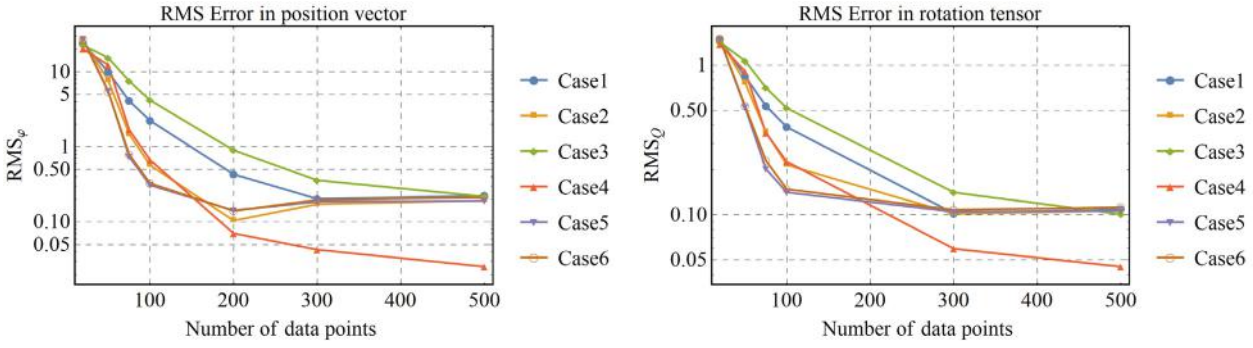

(a) *RMS error in the position vector* (b) *RMS error in the rotation tensor*

Fig. 13. RMS error in the approximated configuration space considering no noise in the data obtained from the sensors.

obtain the position vectors of two curves constituting the double helix as $\boldsymbol{\varphi}_1(\xi_1)$ and $\boldsymbol{\varphi}_2(\xi_1)$ as,

$$\begin{aligned}\boldsymbol{\varphi}_1(\xi_1) &= \boldsymbol{\varphi}(\xi_1) + r\boldsymbol{Y}_g(\xi_1);\\ \boldsymbol{\varphi}_2(\xi_1) &= \boldsymbol{\varphi}(\xi_1) - r\boldsymbol{Y}_g(\xi_1).\end{aligned} \tag{78}$$

In the equation above, $\boldsymbol{Y}_g(\xi_1)$ represents the constituent vector of GMAF as defined in (26), with the roll angle field given by,

$$\phi_r(\xi_1) = 2\pi c\left(\frac{\xi_1}{l_0}\right). \tag{79}$$

This formulation can be used to generate graphics and defining the reduced geometry of DNA molecule with the curves $\boldsymbol{\varphi}_1(\xi_1)$ and $\boldsymbol{\varphi}_2(\xi_1)$ representing the *sugar-phosphate backbone* and the vector $r\boldsymbol{Y}_g(\xi_1)$ and $-r\boldsymbol{Y}_g(\xi_1)$ showing the *nitrogenous base* pairs.

Fig. 14 shows two examples of double helix intertwining a space curve $\boldsymbol{\varphi}(\xi_1)$. The dotted black curve represents the curve $\boldsymbol{\varphi}(\xi_1)$, the green and red strand (with n being number of strands per cycle) represents the vectors $r\boldsymbol{Y}_g(\xi_1)$ and $-r\boldsymbol{Y}_g(\xi_1)$ respectively. The blue curves shows the curves $\boldsymbol{\varphi}_1(\xi_1)$ (connected to green strands) and $\boldsymbol{\varphi}_2(\xi_1)$ (connected to red strands). Following are the parameters required to obtain the structures in Fig. 14a,

$$\begin{aligned}&l_0 = 500, \quad r = 40, \quad c = 6, \quad n = 16;\\ &\phi_p(\xi_1) = \tfrac{\pi}{2}\sin\left(\tfrac{\pi\xi_1}{l_0}\right).\left(1 - 0.5\sin\left(\tfrac{3.5\pi}{l_0}\right)\right);\\ &\phi_y(\xi_1) = \pi\sin\left(\tfrac{\pi\xi_1}{l_0}\right).\end{aligned} \tag{80}$$

Following are the parameters required to obtain Fig. 14b,

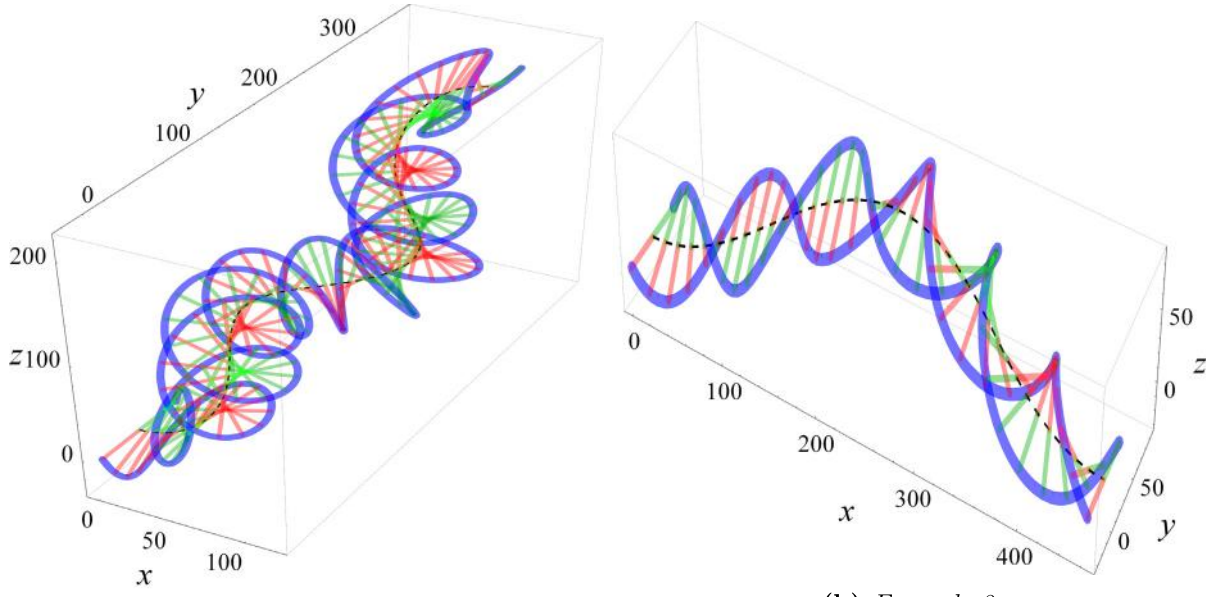

(a) *Example 1* (b) *Example 2*

Fig. 14. Double helix intertwining a space curve.

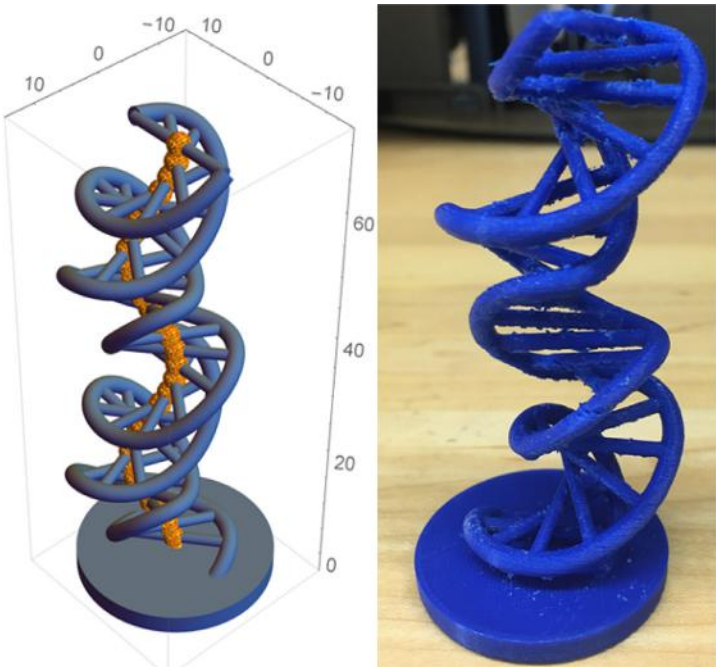

Fig. 15. 3D printed model of double helix.

$$l_0 = 500, \quad r = 35, \quad c = 3, \quad n = 12;$$
$$\phi_p(\xi_1) = \tfrac{\pi}{8}\sin\left(\tfrac{2\pi\xi_1}{l_0}\right); \tag{81}$$
$$\phi_y(\xi_1) = \tfrac{\pi}{8}\sin\left(\tfrac{2\pi\xi_1}{l_0}\right).$$

Animation 1 shows evolution of double helix with changing mid-curve. It is obtained by using dynamic pitch and yaw angle field (say, time dependent). The winding and unwinding effect can be obtained by making $\phi_r(\xi_1)$ dynamic. Fig. 15 shows a 3D printed model of double helix. The beads in the left figure marks the center curve $\boldsymbol{\varphi}(\xi_1)$ (absent in 3D printed model).

6.2. Leaf like structure using RPAF

To obtain a leaf like structure that bears a single manifold character, we first consider a leaf with *node* at origin (node is the point of contact of stem and leaf). The *midrib* of leaf (vein running from the *node* to the leaf *tip*) is given by the curve $\boldsymbol{\varphi}(\xi_1)$, obtained using the pitch and yaw angle fields $\phi_p(\xi_1)$ and $\phi_y(\xi_1)$ with $\xi_1 \in [0, l_0]$. Here, l_0 gives the length of *midrib*.

We generate the *lamina* of leaf as a mesh obtained using *relatively parallel normal vector field* and the inner and outer *margins* of the leaf. We divide the leaf surface into two parts: *lamina* 1 and *lamina* 2. The *relatively parallel normal vector field* $\boldsymbol{M}_1(\xi_1)$ and $\boldsymbol{M}_2(\xi_1)$ with the *generators* $\boldsymbol{M}_{10}$ and $\boldsymbol{M}_{20}$, used to define *lamina* 1 and 2 respectively, are given as

$$\boldsymbol{M}_i(\xi_1) = \boldsymbol{M}_{i0} + [\boldsymbol{Y}_g]_{\phi_r(\xi_1)=\rho_{\mathrm{bi}}(\xi_1)}; \tag{82a}$$
$$\rho_{\mathrm{bi}}(\xi_1) = \rho_{\mathrm{bi}}(0) - \int_0^{\xi_1} \overline{\kappa}_{s1}(k)\mathrm{d}k = \rho_{\mathrm{bi}}(0) - \int_0^{\xi_1} \phi_{y,k}\sin(\phi_p(k))\mathrm{d}k; \tag{82b}$$
$$\boldsymbol{M}_{i0} = \boldsymbol{Q}_g(0)|_{(\phi_r(0)=\rho_{\mathrm{bi}}(0))} \cdot \boldsymbol{E}_2, \text{ with } i = 1,2. \tag{82c}$$

In Eq. (82b), $\rho_{\mathrm{bi}}(\xi_1)$ is obtained using the results (31a) and (34). It represents the roll angle field required to obtain a *relatively normal vector field* (refer Section 4.2). The predefined angle $\rho_{\mathrm{bi}}(0)$ are used to obtain the *generator* $\boldsymbol{M}_{i0}$ using Eq. (82c).

Leaf *margin* essentially represents the outer boundary of the *lamina*. We call that as an outer *margin*, with $\Gamma^1_{\mathrm{outer}}$ and $\Gamma^2_{\mathrm{outer}}$ representing outer *margin* for *lamina* 1 and 2 respectively. In order to mesh the *lamina*, we define inner *margins* with $\Gamma^1_{\mathrm{inner}I}$ and $\Gamma^2_{\mathrm{inner}I}$ representing I^{th} inner *margin* for *lamina* 1 and 2 respectively. The position vectors representing these curves are given by,

$$\boldsymbol{\varphi}_{\Gamma^i_{\mathrm{outer}}} = \boldsymbol{\varphi} + rW(\xi_1)\boldsymbol{M}_i \quad \text{for outer margin of lamina } i; \tag{83a}$$
$$\boldsymbol{\varphi}_{\Gamma^i_{\mathrm{inner}I}} = \boldsymbol{\varphi} + rW(\xi_1)\Psi_I\boldsymbol{M}_i \quad \text{for } I^{\mathrm{th}} \text{ inner margin of lamina } i. \tag{83b}$$

In the equation above, r represents the width parameter of the *lamina*, $W(\xi_1)$ represents the weight function for the outer margin and $\Psi_I \in (0,1)$ is additional weight for the I^{th} inner *margin*. Note that if $\max(W(\xi_1)) = 1$, then r represents the maximum width of *lamina*, similarly, if $W(\xi_1) =$ constant, then all the inner and outer *margins* transforms to *relatively parallel curves* to the *midrib*. Therefore, the width of *lamina* at the arclength ξ_1 is given by $rW(\xi_1)$. Fig. 16 demonstrates the construction discussed so far.

Any other orientation of the leaf defined by $l_0, \phi_p(\xi_1), \phi_y(\xi_1), \rho_{\mathrm{bi}}(0)$, can be obtained by rotating the leaf pivoted at the origin and then translating it as required. The stem of leaf can be obtained by extruding the cross-sections along a space curve.

Fig. 17 shows three different leaves constructed using same $l_0, \phi_p(\xi_1), \phi_y(\xi_1), \rho_{\mathrm{bi}}(0)$ but different weights $W_1(\xi_1), W_2(\xi_1)$ and $W_3(\xi_1)$ and widths r as,

$$l_0 = 6, \quad \rho_{\mathrm{b1}}(0) = 0.7, \quad \rho_{\mathrm{b2}}(0) = 0.7 + \tfrac{5\pi}{9};$$
$$r_1 = r_2 = \tfrac{l_0}{3.5}, \quad r_3 = 0.4; \tag{84}$$
$$\phi_p(\xi_1) = \phi_y(\xi_1) = \tfrac{\pi}{8}\sin\left(\tfrac{\pi\xi_1}{l_0}\right)$$

$$W_1(\xi_1) = 0.5\left(1 + \sin\left(\tfrac{2\pi\xi_1}{l_0} - \tfrac{\pi}{2}\right)\right);$$
$$W_2(\xi_1) = W_1(\xi_1) + \tfrac{2}{75}\sin^2\left(\tfrac{4\pi\xi_1}{l_0} - \pi\right); \tag{85}$$
$$W_3(\xi_1) = f(\xi_1) + \begin{cases} \frac{14\xi_1}{3} & 0 \leqslant \xi_1 \leq 0.75 \\ \frac{-4\xi_1}{3} + 4.5 & 0.75 \leqslant \xi_1 \leq 1.5 \\ \frac{5\xi_1}{6} + 1.25 & 1.5 \leqslant \xi_1 \leq 3 \\ \frac{-3\xi_1}{5} + 3.6 & 3.5 \leqslant \xi_1 \leqslant l_0 \end{cases}.$$

In the equation for the weight W_3 of leaf 3, the function $f(\xi_1)$ represents the triangular wave with the period of 0.16 and amplitude

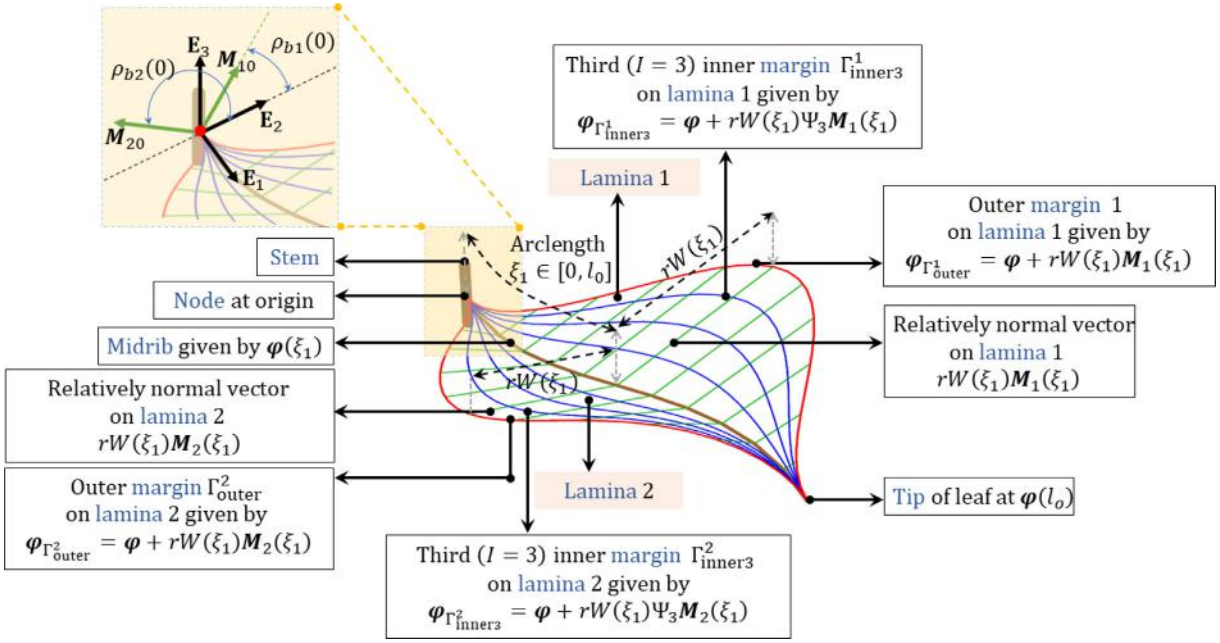

Fig. 16. Geometry of leaf obtained using RPAF.

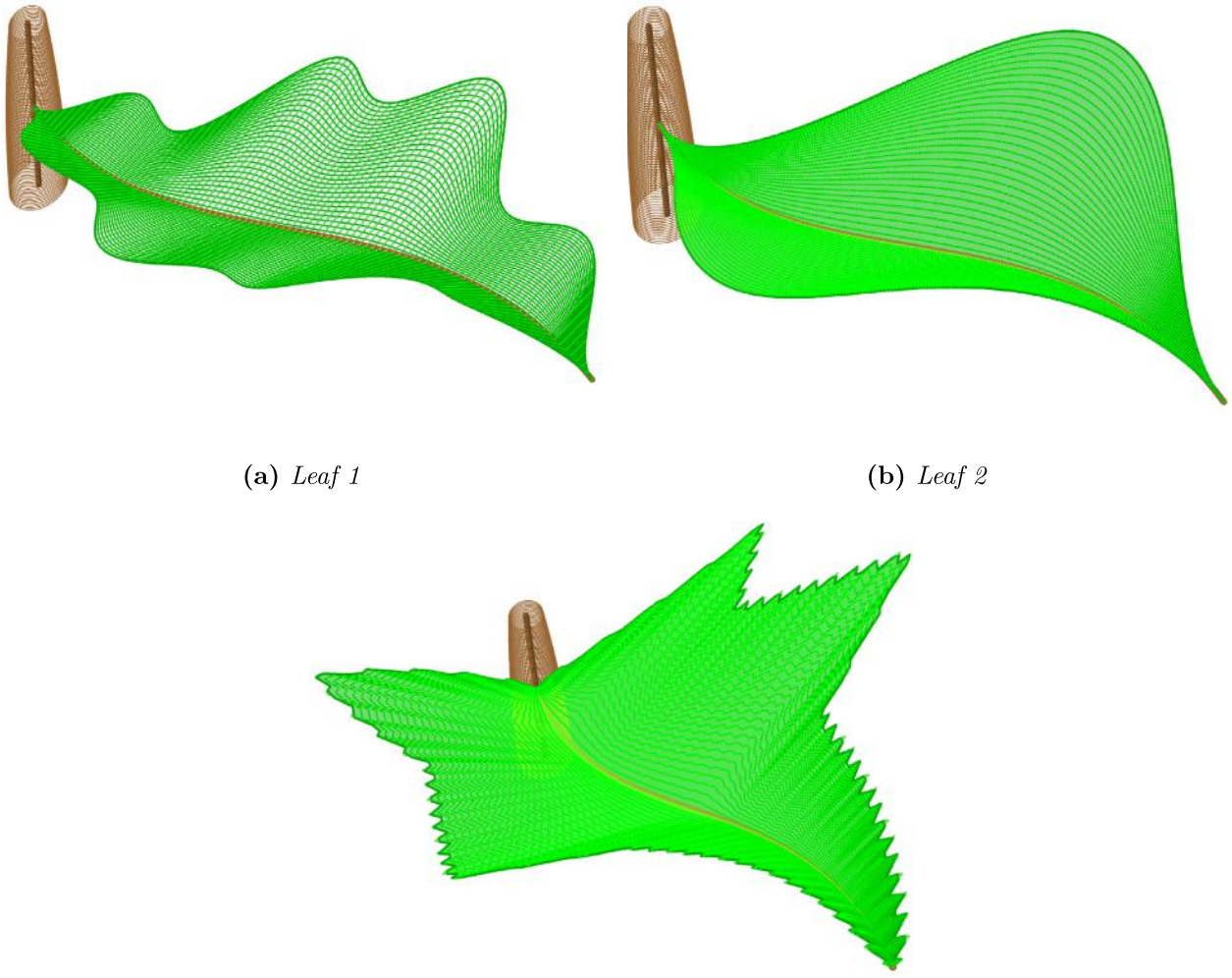

(a) *Leaf 1* (b) *Leaf 2*

(c) *Leaf 3*

Fig. 17. Leaf obtained using same midrib but different weight function.

of 0.084. This is used to generate corrugation and irregularity in the outer margin of the leaf 3 (Fig. 17c).

An entire plant can be generated as shown in Fig. 18. The stems are obtained by extruding circular cross-section varying smoothly along the curves. Leaves of different sizes and orientation are obtained as discussed before.

The dynamic motion in the leaf (say due to wind load) can be graphically obtained by making $\phi_p(\xi_1), \phi_y(\xi_1), \rho_{\text{bi}}(0)$ dynamic. Animation 2 shows the dynamic effect added to leaf (fluttering of leaf).

7. Summary and conclusions

This paper can be broadly summarized into three domains. In the first part, we detail various approaches to curve framing. After a brief discussion on Frenet and RPAF frame and their continuity requirements, we delineate the construction of general material frame MF. We also discuss three approaches to parameterize finite rotations: Euler angle approach, unit quaternion and Rodrigues rotation formula. The relationship between curvature tensor of various frames are obtained.

Secondly, we propose an algorithm to estimate the state space of a single manifold characterized system using a limited set of material curvature and velocity data. The idea is to estimate the material linear and angular velocity data (or equivalently midcurve strain and curvature vector of beam) using various interpolation approaches. This interpolation is consistent as we estimate the material linear and angular velocity field $(\overline{\boldsymbol{v}}^h(\xi_1), \overline{\boldsymbol{\omega}}^h(\xi_1))$ in a linear $so(3)$ plane. We use the approximated fields $(\overline{\boldsymbol{v}}^h(\xi_1), \overline{\boldsymbol{\omega}}^h(\xi_1))$ to first estimate the configuration space $\left(\boldsymbol{\varphi}^h(\xi_1), \mathbf{Q}^h(\xi_1)\right)$ and then the tangent space $(\boldsymbol{v}^h, \boldsymbol{\omega}^h)$. Amongst all the interpolation approaches suggested, the C^{-1} interpolation of material data is special, because it results in a closed form solution to the estimated configuration, and because it leads to the development of curvature dependent shape functions that may be glued together to obtain a smooth global configuration. We call this approach *smooth patch estimation and gluing technique* (SPEG). An interesting method to obtain the solution of SPEG merely by using the idea of parallel-transport is presented. The estimation methods discussed are convergent and free of singularity. An illustration that compares all the approaches and demonstrates the error analysis is presented. We also note that

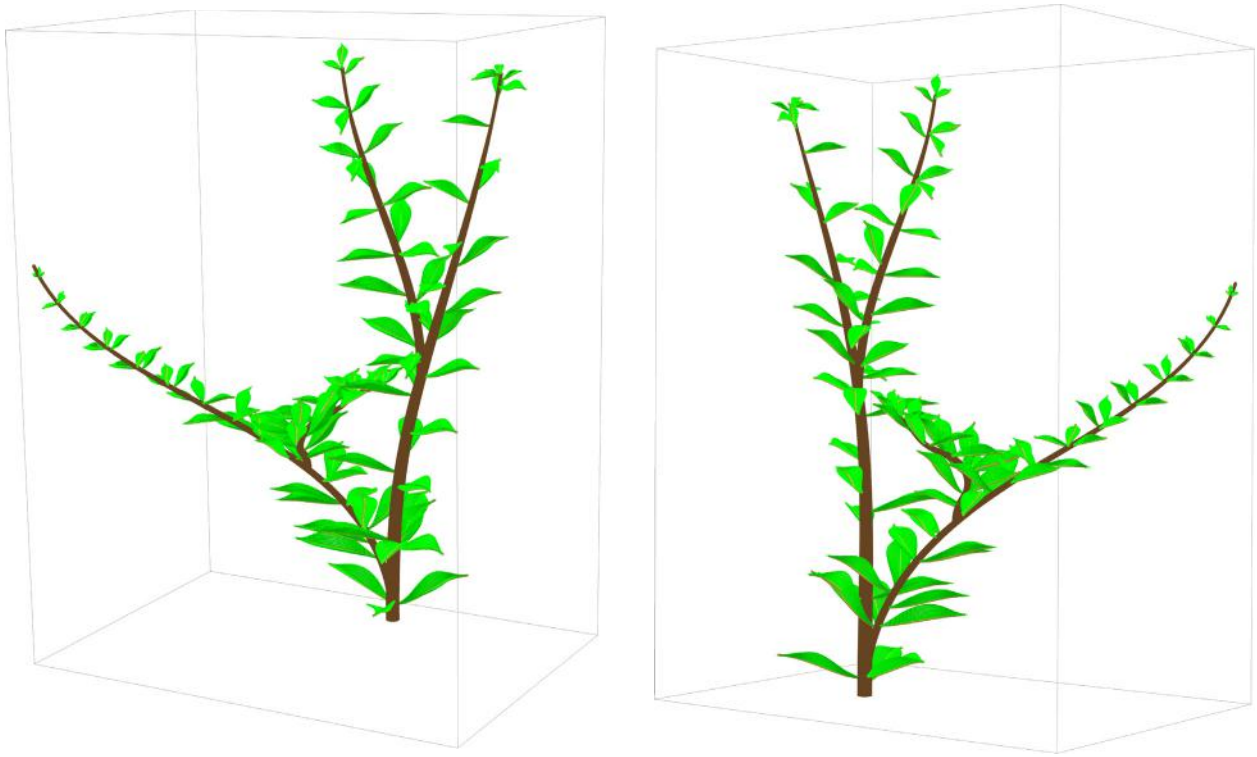

(a) *View 1* (b) *View 2*

Fig. 18. Computer generated plant with varying sizes and orientation of leaves.

the state space of beam and a moving rigid body has similar mathematical nature because both of them are single manifold characterized systems. Thus, we observe the similarity in the problem of path estimation of moving object and the shape sensing of the beam under deformation.

The applications of framed space curves are numerous. Finally, we demonstrate the ability of the framed space curve to develop computer graphics. We do this by presenting the construction of double helix intertwining a space curve using GMAF. We present a second example demonstrating construction of leaves and plant using RPAF.

We anticipate that in the future, we will combine the estimation method developed in this paper with the general kinematics of the Cosserat beam (refer Chadha and Todd [34]) to extend our work in the field of shape reconstruction of slender structures.

Acknowledgements

Funding for this work was provided by the United States Army Corps of Engineers through the U.S. Army Engineer Research and Development Center Research Cooperative Agreement W912HZ-17-2-0024.

Appendix A

A.1. Curvature in terms of unit quaternion parameters and Rodriguez parameters

A.1.1. Curvature in terms of unit quaternion parameters

$$\overline{\kappa}_1 = 2\Big(-q_1 q_{0,\xi_1} + q_0 q_{1,\xi_1} + q_3 q_{2,\xi_1} - q_2 q_{3,\xi_1}\Big); \tag{86a}$$

$$\overline{\kappa}_2 = 2\Big(-q_2 q_{0,\xi_1} - q_3 q_{1,\xi_1} + q_0 q_{2,\xi_1} + q_1 q_{3,\xi_1}\Big); \tag{86b}$$

$$\overline{\kappa}_3 = 2\Big(-q_3 q_{0,\xi_1} + q_2 q_{1,\xi_1} - q_1 q_{2,\xi_1} + q_0 q_{3,\xi_1}\Big). \tag{86c}$$

A.1.2. Curvature in terms of Rodriguez parameters

$$\overline{\kappa}_1 = s_\theta n_{\theta 1,\xi_1} + (1-c_\theta)\big(n_{\theta 3} n_{\theta 2,\xi_1} - n_{\theta 2} n_{\theta 3,\xi_1}\big) + n_{\theta 1}\theta_{,\xi_1}; \tag{87a}$$

$$\overline{\kappa}_2 = s_\theta n_{\theta 2,\xi_1} + (1-c_\theta)\big(n_{\theta 1} n_{\theta 3,\xi_1} - n_{\theta 3} n_{\theta 1,\xi_1}\big) + n_{\theta 2}\theta_{,\xi_1}; \tag{87b}$$

$$\overline{\kappa}_3 = s_\theta n_{\theta 3,\xi_1} + (1-c_\theta)\big(n_{\theta 2} n_{\theta 1,\xi_1} - n_{\theta 1} n_{\theta 2,\xi_1}\big) + n_{\theta 3}\theta_{,\xi_1}. \tag{87c}$$

Note that above set of equations can be obtained by using Eqs. (9) and (11a) or alternatively by substituting $q_0 = c_{\theta/2}, q_i = s_{\theta/2} n_{\theta i}$ where $i = 1-3$, in Eqs. 86a, 86b and 86c.

A.2. Vector coefficient for SPEG technique of state estimation

We represent the vector coefficients in the form given below,

$$\Big[[\boldsymbol{A}_{\overline{n}1}]_{\{\boldsymbol{E}_i\}}, [\boldsymbol{A}_{\overline{n}2}]_{\{\boldsymbol{E}_i\}}, [\boldsymbol{A}_{\overline{n}3}]_{\{\boldsymbol{E}_i\}}, [\boldsymbol{A}_{\overline{n}4}]_{\{\boldsymbol{E}_i\}}\Big]_{3\times 4} = [\boldsymbol{C}_{\overline{n}}]_{3\times 4}[\boldsymbol{A}_{\overline{n}}]_{4\times 4}; \tag{88a}$$

$$\Big[[\boldsymbol{B}_{\overline{n}i1}]_{\{\boldsymbol{E}_i\}}, [\boldsymbol{B}_{\overline{n}i2}]_{\{\boldsymbol{E}_i\}}, [\boldsymbol{B}_{\overline{n}i3}]_{\{\boldsymbol{E}_i\}}, [\boldsymbol{B}_{\overline{n}i4}]_{\{\boldsymbol{E}_i\}}\Big]_{3\times 4} = [\boldsymbol{C}_{\overline{n}}]_{3\times 4}[\boldsymbol{B}_{\overline{n}}]_{4\times 4}; \tag{88b}$$

In the equation above, the notation $[\boldsymbol{A}_{\overline{n}1}]_{\{\boldsymbol{E}_i\}} = [\langle \boldsymbol{A}_{\overline{n}1}, \boldsymbol{E}_1\rangle, \langle \boldsymbol{A}_{\overline{n}1}, \boldsymbol{E}_2\rangle, \langle \boldsymbol{A}_{\overline{n}1}, \boldsymbol{E}_3\rangle]^T$, represents the component of the coefficient vector $[\boldsymbol{A}_{\overline{n}1}]_{\{\boldsymbol{E}_i\}}$ in $\{\boldsymbol{E}_i\}$ frame. Therefore, the approximated solution is expressed in $\{\boldsymbol{E}_i\}$ frame (Note that the boundary conditions were expressed in $\{\boldsymbol{E}_i\}$ frame). The matrix $[\boldsymbol{C}_{\overline{n}}]$ represents the 12 constants of integration corresponding to $\overline{n}^{\text{th}}$ patch and is determined using continuity conditions or the boundary conditions. The matrices $[\boldsymbol{A}_{\overline{n}}]$ and $[B_{\overline{n}i}]$ (for $i = 1,2,3$) contains coefficients that are function of the discrete velocity data $\overline{\boldsymbol{v}}_n$ and $\overline{\boldsymbol{\omega}}_n$.

$$[\boldsymbol{A}_{\overline{n}}] = \begin{bmatrix} \frac{\langle \overline{\boldsymbol{\omega}}_n \times \overline{\boldsymbol{v}}_n, \boldsymbol{E}_1\rangle}{\omega_n^2} & \frac{\langle \overline{\boldsymbol{v}}_n, \overline{\boldsymbol{\omega}}_n\rangle \langle \overline{\boldsymbol{\omega}}_n, \boldsymbol{E}_1\rangle}{\omega_n^2} & -\frac{\langle \overline{\boldsymbol{\omega}}_n \times \overline{\boldsymbol{\omega}}_n \times \overline{\boldsymbol{v}}_n, \boldsymbol{E}_1\rangle}{\omega_n^3} & -\frac{\langle \overline{\boldsymbol{\omega}}_n \times \overline{\boldsymbol{v}}_n, \boldsymbol{E}_1\rangle}{\omega_n^2} \\ \frac{\langle \overline{\boldsymbol{\omega}}_n \times \overline{\boldsymbol{v}}_n, \boldsymbol{E}_2\rangle}{\omega_n^2} & \frac{\langle \overline{\boldsymbol{v}}_n, \overline{\boldsymbol{\omega}}_n\rangle \langle \overline{\boldsymbol{\omega}}_n, \boldsymbol{E}_2\rangle}{\omega_n^2} & -\frac{\langle \overline{\boldsymbol{\omega}}_n \times \overline{\boldsymbol{\omega}}_n \times \overline{\boldsymbol{v}}_n, \boldsymbol{E}_2\rangle}{\omega_n^3} & -\frac{\langle \overline{\boldsymbol{\omega}}_n \times \overline{\boldsymbol{v}}_n, \boldsymbol{E}_2\rangle}{\omega_n^2} \\ \frac{\langle \overline{\boldsymbol{\omega}}_n \times \overline{\boldsymbol{v}}_n, \boldsymbol{E}_3\rangle}{\omega_n^2} & \frac{\langle \overline{\boldsymbol{v}}_n, \overline{\boldsymbol{\omega}}_n\rangle \langle \overline{\boldsymbol{\omega}}_n, \boldsymbol{E}_3\rangle}{\omega_n^2} & -\frac{\langle \overline{\boldsymbol{\omega}}_n \times \overline{\boldsymbol{\omega}}_n \times \overline{\boldsymbol{v}}_n, \boldsymbol{E}_3\rangle}{\omega_n^3} & -\frac{\langle \overline{\boldsymbol{\omega}}_n \times \overline{\boldsymbol{v}}_n, \boldsymbol{E}_3\rangle}{\omega_n^2} \\ 1 & 0 & 0 & 0 \end{bmatrix} \tag{89}$$

$$[\boldsymbol{B}_{i\overline{n}}] = \begin{bmatrix} \frac{\langle \boldsymbol{d}_{i0}+\overline{\boldsymbol{\omega}}_n\times\overline{\boldsymbol{\omega}}_n\times\boldsymbol{d}_{i0},\boldsymbol{E}_1\rangle}{\omega_n^2} & 0 & \frac{\langle \boldsymbol{d}_{i0}\times\overline{\boldsymbol{\omega}}_n,\boldsymbol{E}_1\rangle}{\omega_n} & -\frac{\langle \overline{\boldsymbol{\omega}}_n\times\overline{\boldsymbol{\omega}}_n\times\boldsymbol{d}_{i0},\boldsymbol{E}_1\rangle}{\omega_n^2} \\ \frac{\langle \boldsymbol{d}_{i0}+\overline{\boldsymbol{\omega}}_n\times\overline{\boldsymbol{\omega}}_n\times\boldsymbol{d}_{i0},\boldsymbol{E}_2\rangle}{\omega_n^2} & 0 & \frac{\langle \boldsymbol{d}_{i0}\times\overline{\boldsymbol{\omega}}_n,\boldsymbol{E}_2\rangle}{\omega_n} & -\frac{\langle \overline{\boldsymbol{\omega}}_n\times\overline{\boldsymbol{\omega}}_n\times\boldsymbol{d}_{i0},\boldsymbol{E}_2\rangle}{\omega_n^2} \\ \frac{\langle \boldsymbol{d}_{i0}+\overline{\boldsymbol{\omega}}_n\times\overline{\boldsymbol{\omega}}_n\times\boldsymbol{d}_{i0},\boldsymbol{E}_3\rangle}{\omega_n^3} & 0 & \frac{\langle \boldsymbol{d}_{i0}\times\overline{\boldsymbol{\omega}}_n,\boldsymbol{E}_3\rangle}{\omega_n} & -\frac{\langle \overline{\boldsymbol{\omega}}_n\times\overline{\boldsymbol{\omega}}_n\times\boldsymbol{d}_{i0},\boldsymbol{E}_3\rangle}{\omega_n^2} \\ 0 & 0 & 0 & 0 \end{bmatrix} \tag{90}$$

Appendix B. Supplementary material

Supplementary data associated with this article can be found, in the online version, at https://doi.org/10.1016/j.compstruc.2019.03.011.

References

[1] Coolidge J. The story of tangents. Am Math Mon 1951;58(7):449–62.
[2] Descartes R. La géométrie. Leiden; 1637.
[3] Euler L. Introductio in analysin infinitorum. MM Bousquet; 1748.
[4] Frenet F. Sur les courbes a double courbure. J Math Pure Appl 1852:437–47.
[5] Serret JA. Sur quelques formules relatives à la théorie des courbes à double courbure. J Math Pure Appl 1851:193–207.
[6] Darboux G. Leçons sur la théorie générale des surfaces; 1894.
[7] A Ivey T, M Landsberg J. Cartan for beginners: differential geometry via moving frames and exterior differential systems, vol. 61. RI: American Mathematical Society Providence; 2003.
[8] Cartan É. La géométrie des espaces de riemann; 1925.
[9] Cartan EJ. On manifolds with an affine connection and the theory of general relativity. Bibliopolis; 1986.
[10] Bishop RL. There is more than one way to frame a curve. Am Math Mon 1975;82(3):246–51.
[11] Hanson AJ, Ma H. Parallel transport approach to curve framing. Indiana University, Techreports-TR425, vol. 11; 1995. p. 3–7.
[12] Xargay E, Kaminer I, Pascoal A, Hovakimyan N, Dobrokhodov V, Cichella A, et al. Time-critical cooperative path following of multiple unmanned aerial vehicles over time-varying networks. J Guid Control Dyn 2013;36(2):499–516.
[13] Zahradová K. Frame defined by parallel transport for curves in any dimension [Bachelor Thesis]. Prague: Czech Technical University; 2016.
[14] Duhem P. Le potentiel thermodynamique et la pression hydrostatique. Annales scientifiques de l'École Normale Supérieure, vol. 10. p. 183–230.
[15] Cosserat E, Cosserat F. Théorie des corps déformables A. Hermann et fils; 1909.
[16] Chadha M, Todd MD. An introductory treatise on reduced balance laws of Cosserat beams. Int J Solids Struct 2017;126:54–73.
[17] Ericksen J, Truesdell C. Exact theory of stress and strain in rods and shells. Arch Ration Mech Anal 1957;1(1):295–323.
[18] Simo JC. A finite strain beam formulation. the three-dimensional dynamic problem. Part i. Comput Methods Appl Mech Eng 1985;49(1):55–70.
[19] Reissner E. On finite deformations of space-curved beams. Z Angew Math Phys ZAMP 1981;32(6):734–44.
[20] Todd MD, Stull CJ, Dickerson M. A local material basis solution approach to reconstructing the three-dimensional displacement of rod-like structures from strain measurements. J Appl Mech 2013;80(4):041028.
[21] Chadha M, Todd MD. A generalized approach for reconstructing the three-dimensional shape of slender structures including the effects of curvature, shear, torsion, and elongation. J Appl Mech 2017;84(4):041003.
[22] Kreyszig E. Introduction to differential geometry and Riemannian geometry. University of Toronto Press; 1968.
[23] Do Carmo MP. Riemannian geometry. Cambridge University Press; 1992.
[24] Chadha M, Todd MD. An improved shape reconstruction methodology for long rod like structures using Cosserat kinematics-including the poisson's effect. Nonlinear dynamics. Proceedings of the 34th IMAC. A conference and exposition on structural dynamics 2016, vol. 1. Springer; 2019. p. 237–46.
[25] Argyris J. An excursion into large rotations. Comput Methods Appl Mech Eng 1982;32(1–3):85–155.
[26] Wilkins DR. William rowan Hamilton: mathematical genius. Phys World 2005;18(8):33.
[27] Klumpp AR. Singularity-free extraction of a quaternion from a direction-cosine matrix. J Spacecraft Rockets 1976;13(12):754–5.
[28] Spurrier RA. Comment on "Singularity-free extraction of a quaternion from a direction-cosine matrix". J Spacecraft Rockets 1978;15(4):255.
[29] Ibrahimbegović A, Frey F, Kožar I. Computational aspects of vector-like parametrization of three-dimensional finite rotations. Int J Numer Meth Eng 1995;38(21):3653–73.
[30] Ben-Ari M. A tutorial on euler angles and quaternions. Israel: Weizmann Institute of Science; 2014.
[31] Diebel J. Representing attitude: Euler angles, unit quaternions, and rotation vectors. Matrix 2006;58(15–16):1–35.
[32] Park FC. Distance metrics on the rigid-body motions with applications to mechanism design. J Mech Des 1995;117(1):48–54.
[33] Huynh DQ. Metrics for 3d rotations: comparison and analysis. J Math Imag Vis 2009;35(2):155–64.
[34] Chadha M, Todd MD. A comprehensive kinematic model of single-manifold Cosserat beam structures with application to a finite strain measurement model for strain gauges. Int J Solids Struct 2019;159:58–76.
[35] Bartels RH, Beatty JC, Barsky BA. An introduction to splines for use in computer graphics and geometric modeling. Morgan Kaufman; 1995.
[36] Lancaster P, Salkauskas K. Surfaces generated by moving least squares methods. Math Comput 1981;37(155):141–58.
[37] Levin D. The approximation power of moving least-squares. Math Comput Am Math Soc 1998;67(224):1517–31.
[38] Belytschko T, Krongauz Y, Organ D, Fleming M, Krysl P. Meshless methods: an overview and recent developments. Comput Methods Appl Mech Eng 1996;139(1-4):3–47.
[39] Chen J-S, Hillman M, Chi S-W. Meshfree methods: progress made after 20 years. J Eng Mech 2017;143(4):04017001.